



RESEARCH ARTICLE

10.1029/2019JD030291

Key Points:

- A novel method is developed to identify emission mechanisms from automatically tracked dust plumes in the central and western Sahara
- Dust plumes across 14 summers are tracked individually and classified probabilistically as low-level jet or cold pool outflow events
- Eighty-two percent of dust pixels are associated with cold pool outflow events, but low-level jets dominate in the highly active Tidihelt Depression

Correspondence to:

T. Caton Harrison,
thomas.catonharrison@keble.ox.ac.uk

Citation:

Caton Harrison, T., Washington, R., & Engelstaedter, S. (2019). A 14-year climatology of Saharan dust emission mechanisms inferred from automatically tracked plumes. *Journal of Geophysical Research: Atmospheres*, 124, 9665–9690. <https://doi.org/10.1029/2019JD030291>

Received 11 JAN 2019

Accepted 3 AUG 2019

Accepted article online 8 AUG 2019

Published online 30 AUG 2019

Author Contributions

Conceptualization: Richard Washington, Sebastian Engelstaedter

Data curation: Sebastian Engelstaedter

Methodology: Richard Washington, Sebastian Engelstaedter

Validation: Richard Washington, Sebastian Engelstaedter

Formal Analysis: Richard Washington, Sebastian Engelstaedter

Investigation: Richard Washington, Sebastian Engelstaedter

Project Administration: Richard Washington

Resources: Richard Washington, Sebastian Engelstaedter

Supervision: Richard Washington, Sebastian Engelstaedter

Writing - review & editing: Richard Washington, Sebastian Engelstaedter

©2019. The Authors.

This is an open access article under the terms of the Creative Commons Attribution License, which permits use, distribution and reproduction in any medium, provided the original work is properly cited.

A 14-Year Climatology of Saharan Dust Emission Mechanisms Inferred From Automatically Tracked Plumes

Thomas Caton Harrison¹ , Richard Washington¹, and Sebastian Engelstaedter¹

¹Climate Research Laboratory, Oxford University Centre for the Environment, Oxford, UK

Abstract The central and western Sahara is the largest source of mineral aerosols during boreal summer, but observed ground-based data are extremely scarce and typically distant from key source regions. Knowledge of dust emission mechanisms has therefore been mostly limited to short-term observations from a point or model approximations. To address this deficiency, dust plumes from the central and western Sahara are classified according to emission mechanism for June, July, and August of 2004–2017 using an automated inference method, which accurately tracks the timing, convective association, and geometry of plumes observed with the Spinning Enhanced Visible and Infrared Imager aboard Meteosat Second Generation satellites. From these characteristics, plumes are classified as either low-level jet or cold pool outflow events. The extensive data set is used to generate the largest available climatology of dust emission sources and Saharan emission mechanisms. Automated inference compares well with ground-based measurements from the Fennec Campaign (76% accuracy) as well as with an entirely manual approach (88% accuracy). Cold pool activity accounts for 82% of total observed dust and 88% at the point of emission. Dust from cold pools evolves seasonally from hot spots around the Mali-Niger-Algeria border triple point toward the central Sahara to the northwest, while dust from low-level jets is organized along the axis of the northeasterly Harmattan, and dominates emission within the Tidihelt Depression of central Algeria. The widespread importance of cold pool outflows in this research supports the findings of the Fennec Campaign, but low-level jets remain highly significant in certain isolated hot spots.

1. Introduction

Mineral dust is a highly abundant atmospheric aerosol (Boucher et al., 2013; Choobari et al., 2014; Zender et al., 2004), and its variable emission, transport, and deposition affect the planet's radiative budget, human health, meteorological dynamics, and biogeochemical cycles. Of the yearly global dust burden, 40–60% originates in the numerous sources of the Sahara (Engelstaedter et al., 2006), from which emissions peak during boreal summer (Prospero et al., 2002; Schepanski et al., 2007; Washington et al., 2003).

Information about local emission processes in the Sahara is desirable given the high values of dust loadings at low to mid atmospheric levels proximate to dust emission. However, active source regions within the central Sahara suffer from a severe lack of systematic long-term in situ observations with which to constrain emission characteristics (Allen et al., 2013; Garcia-Carreras et al., 2013; Marsham et al., 2013). It is not surprising that dust emission in global climate models is highly divergent with emission totals varying by more than a factor of 5 (Huneeus et al., 2011). Furthermore, little evidence has been found that global climate models used in the Fifth Assessment Report of the IPCC faithfully reproduce any important components of North African emissions or transport (Evan et al., 2014).

Given the approximately cubic dependence of emissions upon wind speed, a crucial element to which dust models are sensitive is the wind field used to drive them (Fiedler et al., 2016; Knippertz & Todd, 2012; Menut, 2008; Woodward, 2011). For emission of dust, winds capable of exceeding local emissions thresholds are needed (Bagnold, 1941). These winds are embedded within a hierarchy of active processes. At the synoptic scale, these include wind regimes such as the Harmattan, Atlantic inflow, and monsoon flow, as compared by Chaboureaud et al. (2016). Describing these regimes helps to explain the underlying meteorological conditions associated with dusty conditions on a particular day. However, the short-term processes generating the high winds directly responsible for uplift of dust usually operate below the synoptic scale

(Tegen & Schulz, 2014), meaning observation and model products that do not at least resolve the mesoscale are ill suited to study their behavior. Reanalysis products typically used for this purpose have been found to underestimate the amplitude of the diurnal cycle of winds in the central Sahara (Allen & Washington, 2014; Roberts et al., 2017).

The primary mesoscale meteorological drivers of dust source activation are nocturnal low-level jet (LLJ) breakdown and cold pool outflows (CPOs) from deep convection. The importance of these two key emission mechanisms has been shown with observations from the Fennec field campaign at Bordj-Badji Mokhtar during June 2011, where an analysis of locally emitted and advected dust found that only a tiny contribution (3%) was made by dry convective plumes, with CPOs and LLJs playing the dominant role (Allen et al., 2013). A better understanding of the relative role of these two emission mechanisms and where they operate with respect to major Saharan dust sources would help explain interannual and intraseasonal dust emission variability and allow a directly process-based improvement of dust models. Critical to this is information about emission mechanisms with the spatiotemporal resolution capable of linking wind processes directly to localized dust sources.

Existing estimates of the relative role of LLJs and CPOs from the Fennec campaign are based upon information collected at one point in space, during only 1 month of boreal summer (Allen et al., 2013; Marsham et al., 2013). Partitioning of summertime emissions by LLJs and CPOs on a broader scale is also available from Marsham et al. (2011; 50% CPO) and Heinold et al. (2013; 40% CPO, 40% LLJ and 20% residual). However, these are derived from model simulations without observational evidence to support modeled CPO frequency, seasonality, distribution, or strength in the central Sahara. We aim to address this observational gap.

1.1. Low-Level Jets

LLJs (Figure 1a) are thought to operate across the Sahara (Fiedler et al., 2013; Schepanski et al., 2009). Decoupling from surface momentum fluxes allows winds above the nocturnal boundary layer to become supergeostrophic as they oscillate around geostrophy (Blackadar, 1957). Subsequent initiation of buoyancy-driven turbulence after sunrise by incoming solar radiation mixes this momentum to the surface, driving high winds, which in the Sahara typically peak in the hours after sunrise and before noon (Parker et al., 2005).

Methods to characterize LLJ activity depend upon the data set used. In situ observations, while constrained to study locations, often afford a vertical component to which detection criteria can be applied. These make use of balloon, radiosonde, and wind profiler data where available (Allen & Washington, 2014; Bain et al., 2010; Vanderwende et al., 2015; Washington et al., 2006) and are a valuable insight into jet frequency and strength for short time periods. As their spatial extent is small, however, few inferences can be made about LLJ activity across dust emission regions. Broader climatologies are obtained using model and reanalysis methods (Fiedler et al., 2013; Ge et al., 2016; Heinold et al., 2015; Ranjha et al., 2013; Soares et al., 2014), although in the context of dust emission these are limited by relatively poor reanalysis performance over remote desert regions (Allen & Washington, 2014; Koren & Kaufman, 2004; Roberts et al., 2017).

Aside from cloud motion vector and scatterometer methods to detect LLJs over oceans (Chelton et al., 2000; Garreaud & Muñoz, 2005; Mahajan et al., 1989), satellite observations of LLJs are less common. Over land, one approach to identifying and quantifying LLJ winds has been to track plumes observed in high-resolution satellite overpasses (Koren & Kaufman, 2004; Todd et al., 2008). Without an automated approach, this is a time-consuming and subjective method. To link LLJs to dust emission on a large scale, remotely sensed dust emission events have been classified according to their timing (Schepanski et al., 2009; Tegen et al., 2013). Events occurring during the morning are more likely to be driven by LLJ activity due to the consistent diurnal cycle of momentum mixdown. However, this approach is apt to overestimate the LLJ contribution where other mechanisms also operate (Allen et al., 2013). To date, it has also been limited to manual data sets of tracked satellite-observed plumes. A more advanced automated method for studying LLJ dust emission on a large spatiotemporal scale is therefore needed.

1.2. Cold Pool Outflows

CPOs (Figure 1b) in the vicinity of deep convection (termed “haboobs” when they cause dust storms) are also a major supplier of dust-emitting winds (Bou Karam et al., 2008; Marsham et al., 2008). These occur as convective downdrafts reach the surface and fan out radially as density currents. Observations collected during the Fennec Campaign indicate that CPOs play the dominant role in emission of dust during the Saharan dust maximum in summer (Allen et al., 2013), and manual tracking of these events by satellite shows that

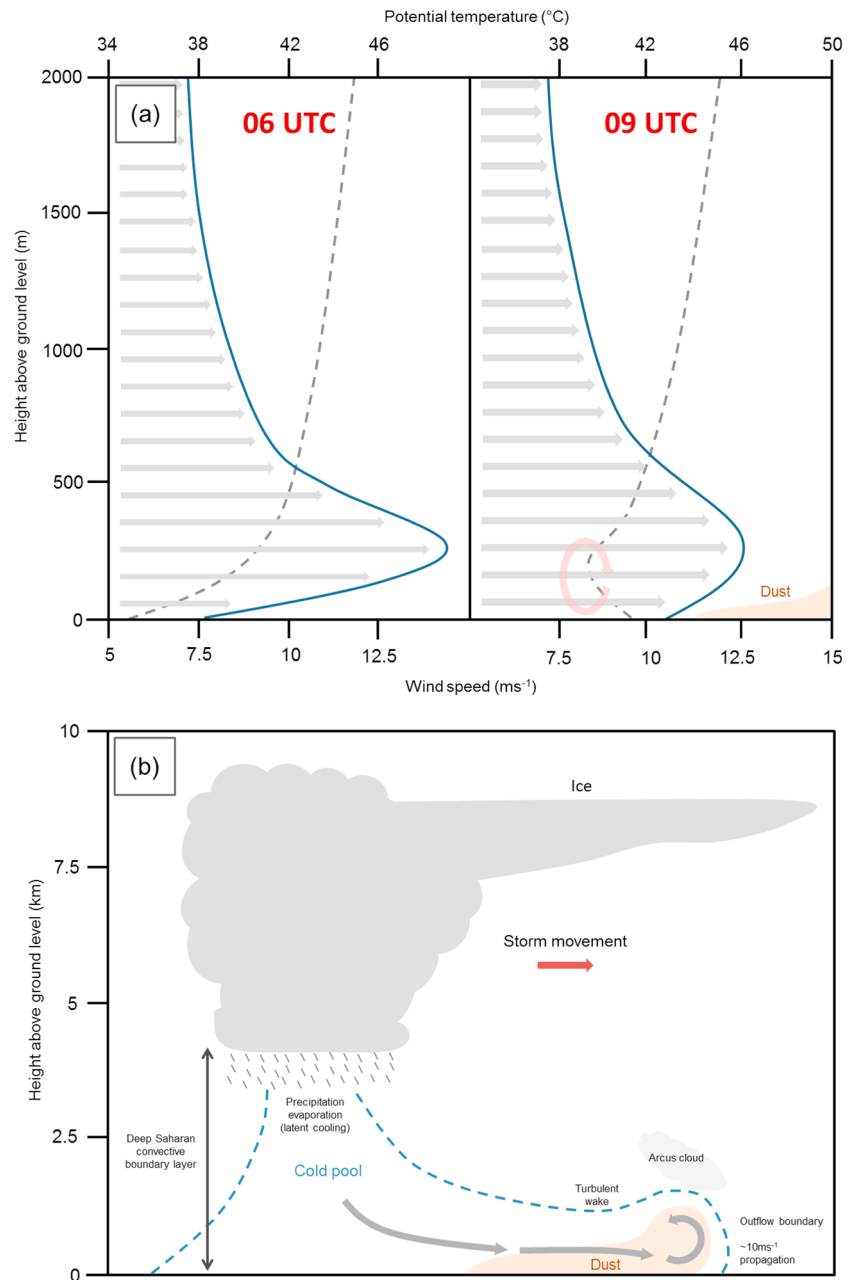


Figure 1. Schematic diagrams of emission mechanisms. (a) shows the nocturnal low-level jet (described in section 1.1) as typical summertime central Saharan wind (solid blue) and potential temperature (dashed gray) profiles at 0600 UTC (left panel) and 0900 UTC (right panel). Convective turbulence in the morning mixes momentum from aloft to the surface, raising dust. (b) shows the mechanics of a cold pool outflow (described in section 1.2) associated with a mature convective system, with the cold pool region delineated in dashed blue.

they can encourage reinitiation of deep convection in the central Sahara where convective inhibition is high (Trzeciak et al., 2017). Although the bulk of outflow events are associated with the West African Monsoon (WAM), CPOs are also observed south of the Atlas mountain range where orography enhances convection (Emmel et al., 2010; Redl et al., 2015). Limited observations of these phenomena and their absence from models with parameterized convection lead to significant moisture transport and dust misrepresentation (Garcia-Carreras et al., 2013). Both CPO and LLJ activities are thought to be controlled in part by displacements of the Saharan heat low (Cuevas et al., 2017; Knippertz & Todd, 2010), which during summer migrates along an east-west axis (Todd et al., 2013).

Building upon early observations of North African haboobs (e.g., Lawson, 1971; Sutton, 1925), studies supported by remote sensing have become the norm (Allen et al., 2013; Emmel et al., 2010; Knippertz et al., 2007; Miller et al., 2008; Provod et al., 2016; Roberts & Knippertz, 2014; Redl et al., 2015). Satellite observations aid in the identification of CPOs and in linking them to deep convective activity. However, each of these studies has focused upon small case study regions, meaning little information is available about cold pool activity across the Sahara as a whole and its relative importance in different dust-emitting locations. Model experiments capable of resolving CPOs can fill this gap (Heinold et al., 2013), but lack systematic cold pool observations for validation and are typically short duration model runs owing to the computational demand of the high spatial resolution. A climatology of CPO dust with wide spatiotemporal coverage derived from identification of cold pool dust emission events is clearly desirable.

1.3. Aims

This study focuses upon the central and western Sahara (CWS), which supplies the bulk of Saharan dust output during boreal summer. To quantify the role of emission mechanisms in the Sahara directly, comprehensive observations of emission events close to source are needed. Ground-based observations are unable to fulfill this role and are unlikely to in the forthcoming decades. Methods to automate the identification and tracking of dust in Spinning Enhanced Visible and Infrared Imager (SEVIRI) imagery (Ashpole & Washington, 2013b) do allow information on dust presence and emission drivers to be collected over long periods. Using quantifiable characteristics of automatically tracked plumes, the present study describes a more accurate method of inferring emission mechanisms for individual plumes. Being fully automated, we are able to apply the method to boreal summer over the period 2004–2017, providing observations of emission sources and processes of unprecedented length. This study aims to

1. accurately automate classification of SEVIRI-observed dust plumes in the CWS as either LLJ- or CPO-driven events,
2. quantify the relative contribution of LLJs and CPOs to the total dust pixels observed using SEVIRI for June, July, and August of 2004–2017, and
3. distinguish LLJ and CPO dominated source regions in the CWS.

Section 2 describes the approach used to delineate dust within SEVIRI, section 3 demonstrates how automatically tracked plumes can be accurately classified, and section 4 validates the methodology. Finally, a climatology of LLJ and CPO dust is presented in section 5.

2. Detecting and Tracking Emitted Dust From Satellite

Brightness temperatures from the SEVIRI aboard Meteosat Second Generation are used here for studying individual dust plumes as imagery is available at 3-km resolution (at nadir) with 15-min temporal resolution. We adopt the “SEVIRI dust flag” (SDF) approach of Ashpole & Washington (2012, 2013b) to identify regions of dust plume presence and track their evolution. The thresholding approach applied to the brightness temperatures is described therein and follows the frequently exploited sensitivity of differences between the 12.0-, 10.8-, and 8.7- μm channels to dust (Ackerman, 1997; Ashpole & Washington, 2012; Lensky & Rosenfeld, 2008; Schepanski et al., 2007), yielding false color images where dust presence is represented by pink colors (Figure 2a). Red regions represent cirrus clouds (e.g., over deep cumulonimbus convection), while lower clouds appear in orange and dark blue. During the day, the blue channel tends to saturate over the dry desert surface. Further discussion of the components of pink dust composites and the visibility of dust layers is found in Ashpole and Washington (2012).

Following Ashpole and Washington (2012), no information about dust quantity such as aerosol optical depth (AOD) is available from SDFs; only the presence or absence of dust (Figure 2b). Although the thresholds from which the dust flags were derived have been carefully tuned to AOD measurements from Aerosol Robotic Network (Holben et al., 1998) stations, the magnitude of threshold exceedance is also affected by total column water vapor, lapse rate, dust top height, size distribution, particle shape, and refractive index (Banks et al., 2018; Brindley et al., 2012).

The tracking of dust plumes used in this paper largely follows the approach described in Ashpole and Washington (2013b), whereby a discrete detected plume from one 15-min time step is traced into the next time step if a spatial overlap is found. When multiple plumes merge, they become part of the largest contributor (in terms of pixel coverage). The capacity of this method to track plumes through time presents the

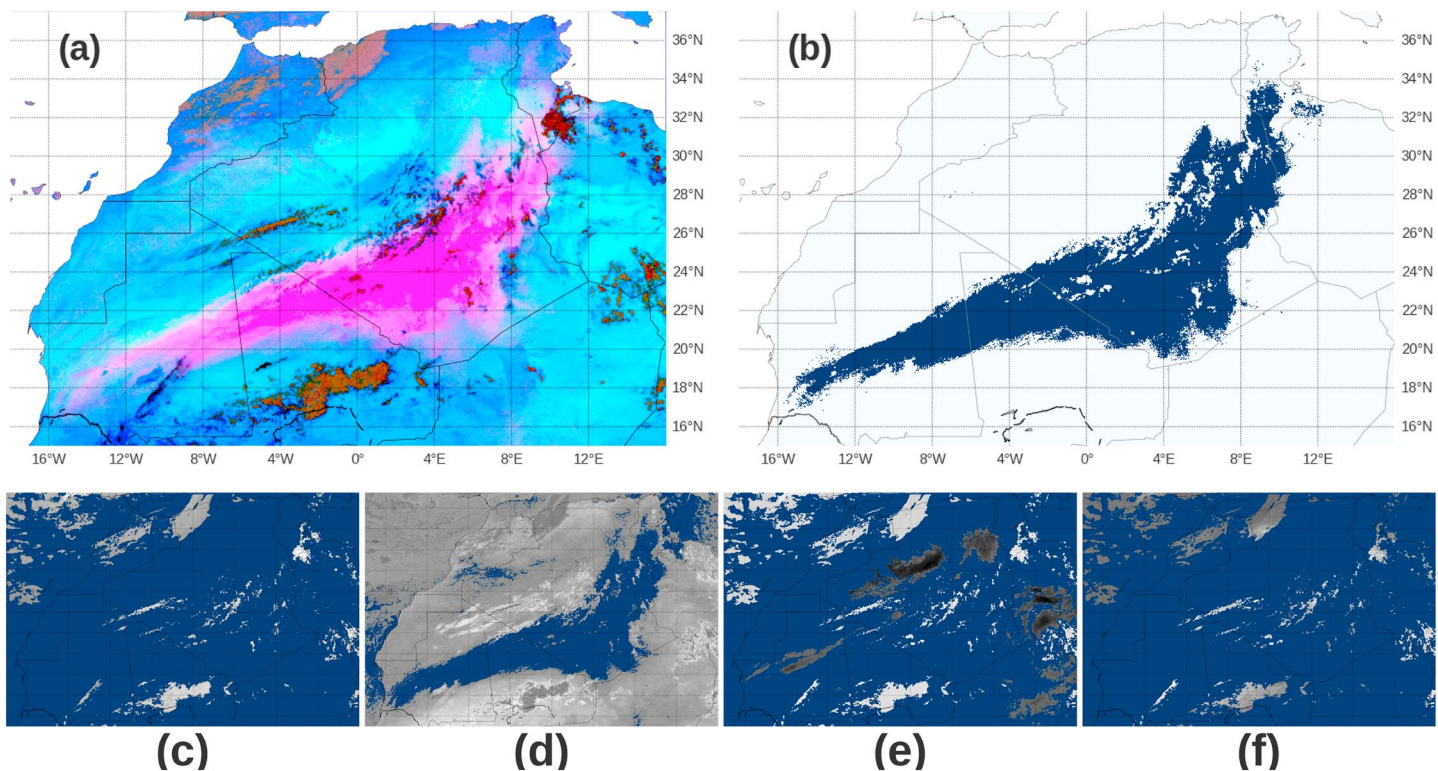


Figure 2. Example of Spinning Enhanced Visible and Infrared Imager dust flags applied to 1100 UTC Spinning Enhanced Visible and Infrared Imager retrievals on 11 June 2010, when a large plume stretched across the entire central and western Sahara. The “pink dust” RGB composite produced from the 8.7-, 10.8-, and 12- μ m channels is shown in (a), with flagged dust pixels (blue) only shown in (b). Pink regions in (a) are dust, with red and orange indicating cloud. The desert surface during the day appears in bright blue.

opportunity to derive methods to establish the signatures of their driving emission mechanism, such as LLJs and CPOs.

Several adjustments have been made to the Ashpole and Washington (2013b) dust tracking scheme in order to better serve inference of plume emission mechanisms. First, the spatial resolution of plume detection is increased from 250 to 50 pixels, meaning plumes are allowed to reach a minimum size of 50 pixels if they exceed 250 at some point in their lifetime. This allows plumes to be tracked slightly further back to source regions and maximizes the detection of their entire life cycles. Furthermore, it addresses the small number of plumes that flicker above and below the detection threshold (leading to false detections of emission). To test the usefulness of this change, 60 plumes in the existing dust tracking scheme were compared with imagery from SEVIRI. Of the total pixels across this period marked as being associated with dust emission (the first time step of a plume's life cycle), 5.8% were found to be caused by a false detection from where an existing plume flickered below the 250 pixel size threshold. The new system with the adjustment described here was found to remedy 75% of these false emission cases.

An important caveat of the SDF method is the reduced capacity to observe nocturnal plumes, as it relies on an atmospheric lapse rate, which renders dust plume tops thermally distinct from the desert surface. This often means that plumes that have aged overnight are falsely detected as new in the morning. Previous work using automatic tracking of SDFs (Ashpole & Washington, 2012, 2013b) has made little use of the timing of plume emission, focusing instead upon climatological and seasonal dust statistics. However, the observed timing of dust emission is a useful quantity with which to infer the driver of uplift (section 3.3). In this paper, therefore, we attempt to partially address this issue by maximizing nocturnal detection.

Visual inspection of SEVIRI “pink dust” imagery reveals regions of dust observable by eye (Figure 3, leftmost panels). However, several of these emission events appear to go undetected by SDF in the early morning hours, as shown in the central column of panels in Figure 3. Missing events are all CPOs, observed in central Mali in Figure 3a, around the Algeria-Niger border in Figure 3b, in southern Algeria in Figure 3c, and along

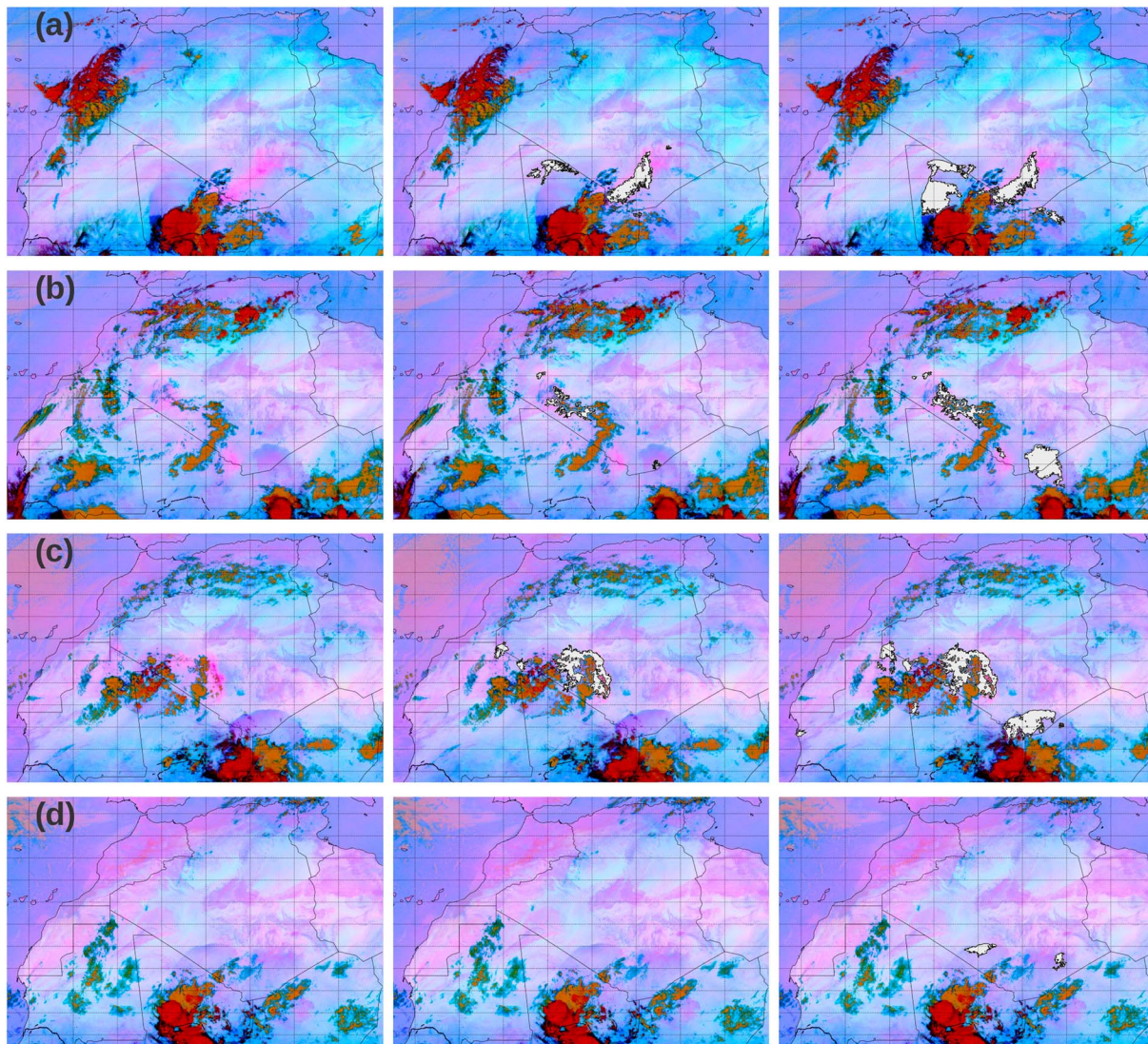


Figure 3. Examples of improvements to dust flagging introduced with an adjusted plume tracking system, showing the raw pink dust composite (left), the original Ashpole and Washington (2013b) flagged image (center), and the result of the improved method (right). Pixels flagged as dust are shown for both old and new algorithms with a white mask. Examples are shown for (a) 19 June 2011 at 0700 UTC, (b) 03 July 2012 at 0200 UTC, (c) 06 July 2012 at 0200 UTC, (d) 29 July 2012 at 0200 UTC.

the Algeria-Mali border in Figure 3d. Thresholds used for SDF detection in Ashpole and Washington (2012) were empirically tuned to delineate dust presence while avoiding false detections from features such as cloud edges or maritime stratus (which can produce similar radiative signatures). Uniformly applying a more generous set of thresholds would therefore be inappropriate. However, analysis of case studies shows that a BT $12.0\text{--}10.8\text{-}\mu\text{m}$ threshold of -1.5 K instead of 0 K reveals previously unobserved nocturnal dust when applied overnight. In our updated plume tracking scheme, we apply this modified threshold only to plumes detected overnight. To avoid additional spurious detection in this scheme, dust flagged using these relaxed threshold must fulfill two conditions not to be discarded. First, emission must take place between 2300 and 0800 UTC. Second, the plume must overlap at some point during its lifetime with the one detected using the original, stricter SDF scheme (i.e., the largest effect of this modification is to track morning plumes back further into the night). The new scheme is successful at backtracking aged plumes, which would have been falsely detected as new, providing a more realistic emission time estimates (Figure 3, rightmost panels).

To test the effect of the new scheme upon plumes on an aggregate scale, we manually identified plumes from June 2011, which were falsely detected late (i.e., an aged plume detected as a new one). Fifty-one cases were found, comprising 8% of the total events. This is likely an underestimate as some plumes will be entirely

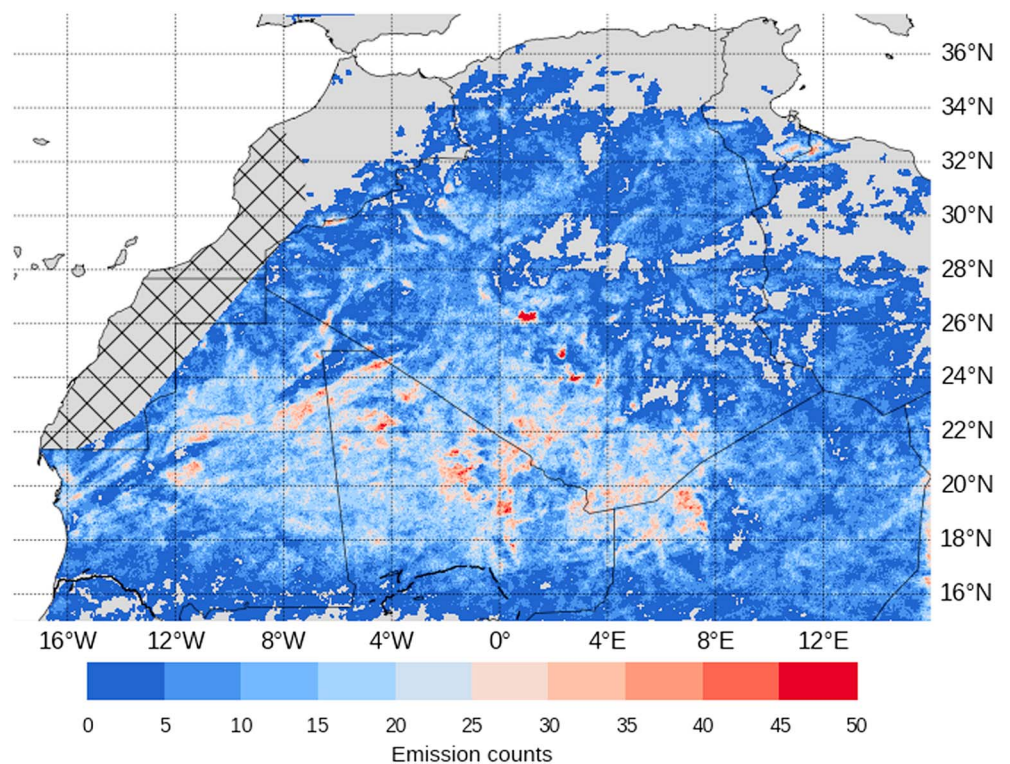


Figure 4. Total counts of dust plume emission events in the Central and Western Sahara for June, July, and August of 2004–2017. A plume emission event is identified as the pixels covered by a plume during the first time step of its lifetime. Map is constructed using the adjusted plume tracking approach described in section 2. The western region of the central and western Sahara along the coast of the Atlantic is masked (hatched area) following Ashpole and Washington (2013b), as this region is prone to false detections due to incursions of marine stratocumulus.

indistinguishable from the relatively cool nocturnal desert surface. The updated scheme fixes 32 (63%) of the erroneous cases, without introducing false alarms. Combined with reduced plume flickering as described above, this updated scheme significantly improves confidence in the timing of emission events.

Close correspondence between sources identified with updated SDFs and the plume source map developed in Ashpole and Washington (2013b) is found when the improved plume tracking method described above is applied to track dust plumes back to their source, with a clear Tidihelt region signal, as well as prominent sources around the Mali-Niger-Algeria triple point, at 19° N, 5° E (Figure 4). Smaller peak emission locations are due to the relaxation of the plume size constraint (from 250 to 50 pixels).

In this paper, plumes are automatically tracked using the method described above for the period of June, July, and August of 2004–2017. Next, each individual plume is analyzed individually in order to infer the driving emission mechanism.

3. Classifying Observed Dust Plumes by Emission Mechanism

3.1. Manual Classification

In order to determine the emission mechanisms responsible for dust plumes, several physical principles are used by the observer. These principles may, in turn, be used to train an automated method. Here, a case study from 2011 is used to demonstrate how emission mechanisms may be identified by eye.

As described with observations collected during the Fennec Campaign (Allen et al., 2013), on the 17 June 2011, the Saharan heat low was centered over the eastern CWS (northern Niger and southern Algeria) and was collocated with a deep dust layer mixed well into the atmospheric boundary layer up to 6 km (Ryder et al., 2015). Allen et al. (2013) identify the large southern dust feature delineated in Figure 5 around the Mali-Niger-Algeria triple point (19° N, 5° E) as a cold pool originating from a mesoscale convective complex, showing that its lofted dust was responsible for one of largest dust detection signals at Bordj-Badji Mokhtar. Inspection of the imagery reveals a sharp boundary in low- and high-level dust, propagating radially away

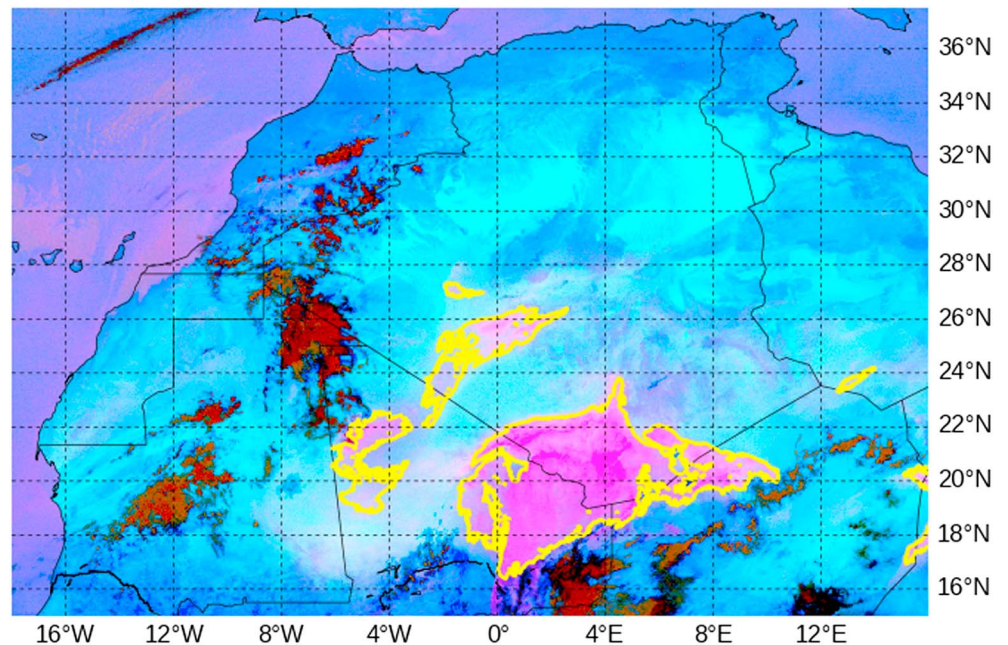


Figure 5. Plumes observed in Spinning Enhanced Visible and Infrared Imager pink dust composites at 1200 UTC on 17 June 2011. Dust detected by the scheme used in section 2 is delineated in yellow.

from a deep convective system in the early hours of the morning. This spreading behavior is typical of a density current, where a dense fluid undercuts another and is followed by turbulent conditions (Simpson, 1969), here capable of lofting dust due to high gusty winds at the outflow boundary. The nocturnal timing of the events reflects the diurnal cycle of convection, with the strongest evaporative downdraft formation occurring in the evening (Garcia-Carreras et al., 2013). Surface fluxes during the day may also play a role in slowing the advance of daytime cold pools or hastening their erosion (Gentine et al., 2016; Huang et al., 2018; Ross et al., 2004). The presence of arcus clouds along some regions of the observed outflow boundary is indicative of cold pool advance and suggests relatively high moisture availability (Marshall et al., 2008). The spatial coherence of the feature is notable, and uplift of dust is organized perpendicular to the direction of the haboob's northwestward travel, typical of the advancing “wall” phenomenon they exhibit (Roberts & Knippertz, 2012).

The LLJ example shown for 17 June 2011 is visible as the northernmost dust features delineated in Figure 5 in western Algeria. Ryder et al. (2015) identify a sharp downward mixing of momentum in operational forecasts for the day over northern Mali, consistent with the nocturnal jet cycle, and suggest that the low-level winds are likely to have been deflected by the Hoggar mountains (22° N, 5° E). This down-mixing of momentum is a result of solar heating, as thermal eddies begin to mix the previously stable nocturnal boundary layer. A series of streak-like structures in lofted dust, visible by noon, is seen propagating southwestward along the Harmattan channel. These include uplift over northern Mali and in the Tidihelt region of central Algeria. The timing, spatial structure, and lack of nearby deep convection make this a clear LLJ case, therefore, even in the absence of model wind simulations. The typical streak-like appearance of LLJ dust could be due to a combination of orographic channeling and the highly localized nature of deposits of easily deflated material. Most highly active dust sources are likely to be associated with paleolakes and outwash plains (Ashpole & Washington, 2013b) rather than large sand seas, meaning dust source activation is favored at isolated hot spots. Cold pools appear to lift dust in much broader swathes, which may be due to highly effective vertical transport above the cold pool head (Huang et al., 2018). Greater dust altitude in turn makes it easier to observe using SEVIRI, which relies upon the thermal contrast between the dust plume top and the surface.

While some of the features above (such as the presence of arcus clouds) are not straightforward to identify automatically, quantifiable features, including emission timing, proximity to deep convection, and geometry, can act as indicators of a plume's consistency with either the LLJ or CPO visual archetype. This principle informs the method used to automate plume classification.

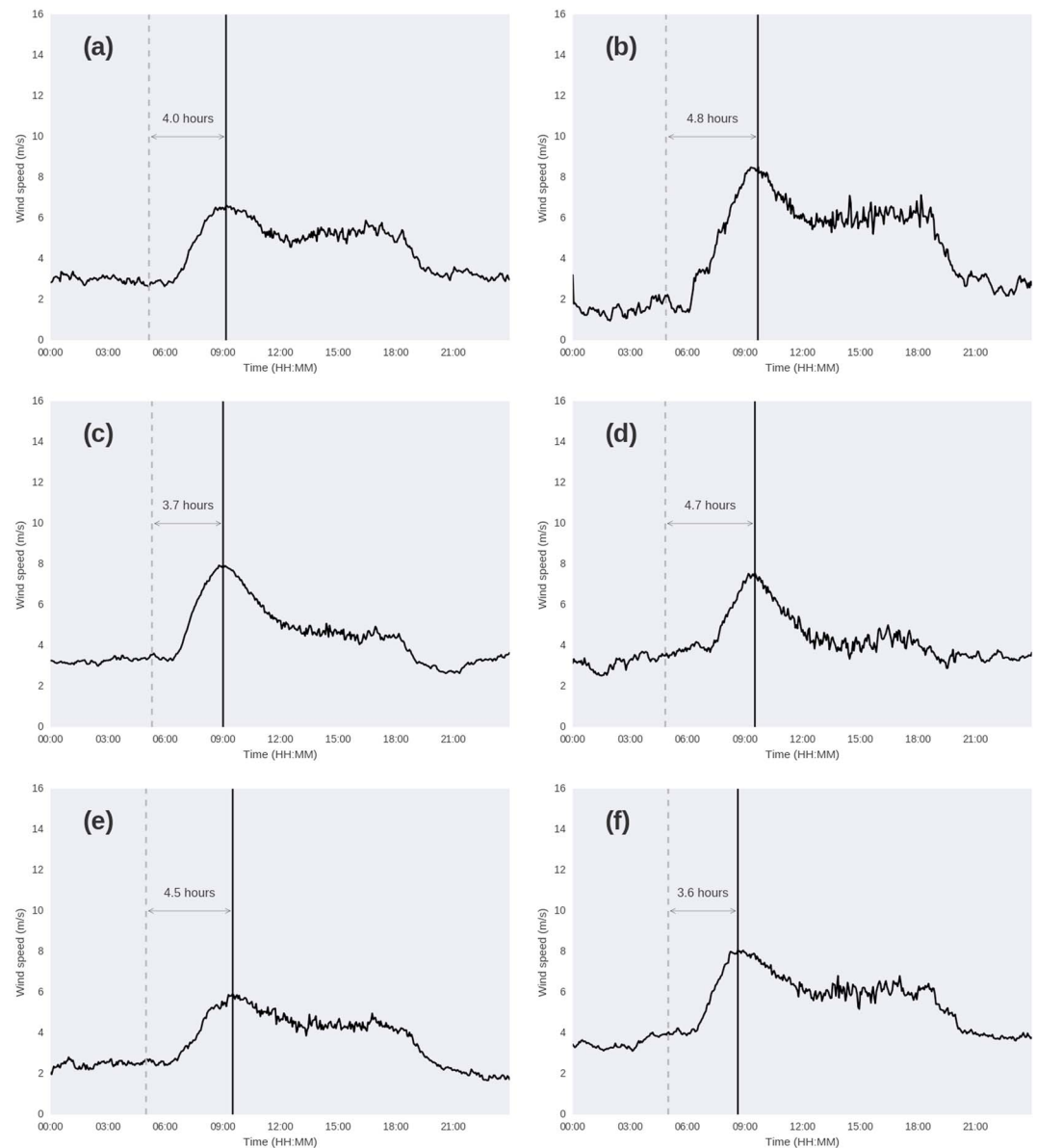


Figure 6. Wind speed composites on days identified as having low-level jet activity, sampled from automatic weather station (a) 131, (b) 133, (c) 134, (d) 135, (e) 138, and (f) 140 (all measured at 2 m above ground level). The black vertical line indicates the mean timing of peak low-level jet momentum winds at the surface. The dashed gray line shows the mean time of sunrise. The interval between the two is marked with a horizontal arrow.

3.2. Automated Classification

The longevity of the dust plume data set available from the tracking scheme described in section 2 can be used to assess the climatological and intraseasonal development of dust emission mechanisms. However, with over 41,000 tracked plumes, manual identification of emission mechanisms becomes challenging and the reproducibility of the subjectively identified mechanisms questionable. While a “deep learning” approach to automated detection is in principle possible, a large training data set would be needed, and the methodology would be opaque. Here, we base an automated approach upon the simple visual principles from section 3.1. Three quantifiable characteristics of the observed dust plumes are used as predictors: the emission timing, the association with deep convection, and the plume geometry.

3.3. Timing of Emission

Emission mechanisms in the CWS tend to follow a diurnal cycle, as described in section 3.1. The most consistent of these is the timing of LLJ emission, as this is controlled in large part by the timing of sunrise.

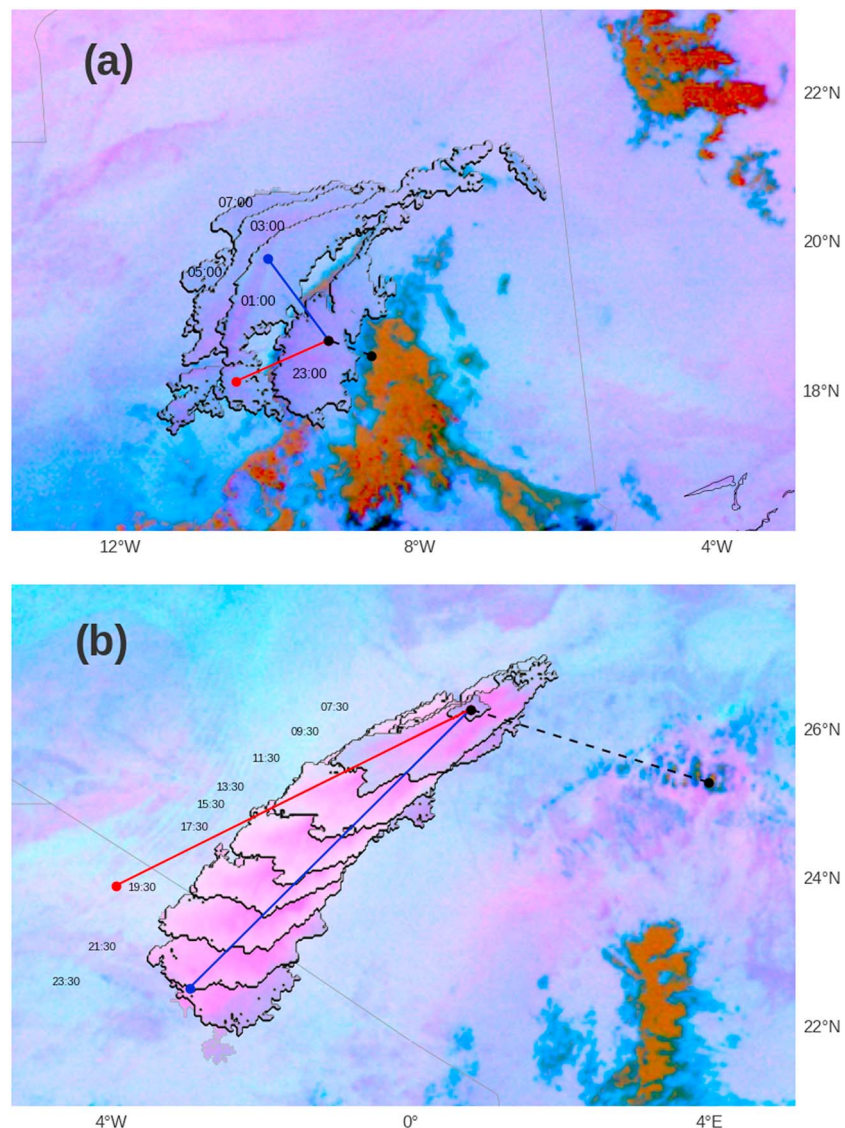


Figure 7. Life cycle of a typical tracked plume (at 2-hourly intervals), shown as a delineated region of the RGB pink dust composite, with each time step overlain (older detections plotted over newer ones). The background shows the pink dust composite at the time of plume emission, that is, 2300 in (a) and 0730 in (b). Labels indicate the UTC time of each time step (first predictor), the black dashed line indicates the distance to deep convection at the point of emission (second predictor), and the blue and red lines indicate the propagation direction and orientation, respectively (third predictor). A cold pool outflow case is shown in (a) with a low-level jet in (b).

As one of the three predictor variables, automatically detected plume emission timing can be compared with the expected peak time for LLJ momentum surface wind speed acceleration. To derive an estimate for the time at which dust activating LLJ winds are expected to peak, we analyze winds observed at 2 m by the Fennec automatic weather station network (Hobby et al., 2013). Following Allen et al. (2015), we detect days on which an LLJ is clearly active by checking for a gradual increase and decrease of winds during the morning, which follows a Gaussian shape.

The time between sunrise and peak LLJ winds is found to vary between 3.6 and 4.8 hr with a mean time of 4.55 hr (Figure 6). Each automatic weather station exhibits a comparable increase toward peak LLJ winds in the morning followed by more variable winds in the afternoon. In each case, a small lag after sunrise of around an hour occurs on average before winds ramp up toward their peak. The station with the largest delay of 4.8 hr after sunrise (133; Figure 6b) appears also to have the lowest average presunrise winds and highest peak LLJ winds. This could indicate greater boundary layer stratification overnight, leading to a

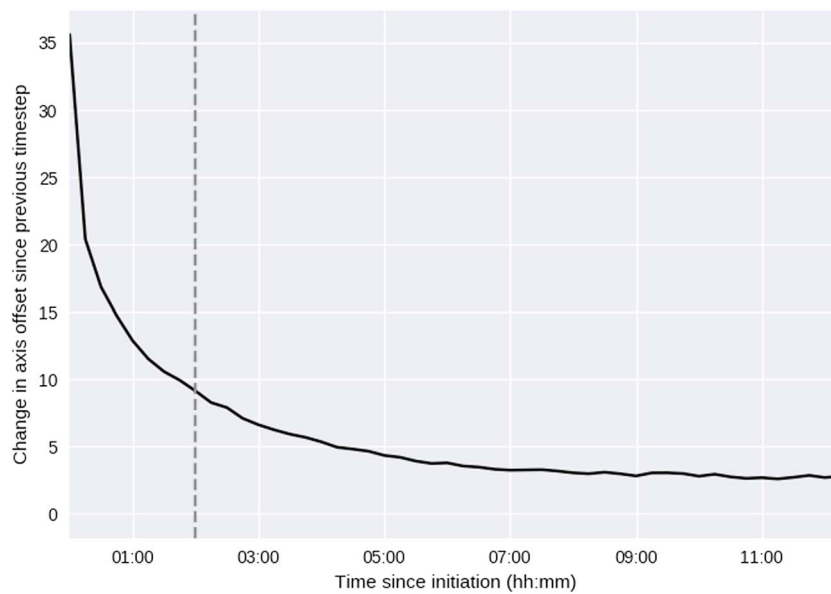


Figure 8. Mean change in the axis offset criterion since it was calculated in the previous time step of a plume's evolution, plotted against the time since the emission of the plume. Calculated from the mean of all plumes from June, July, and August of 2004–2017. The dashed gray vertical line indicates the 2-hr cutoff point before which plume probabilities are not calculated.

more momentum delivered to the surface at sunrise. On the whole, however, variation between stations in this delay is small. We approximate a peak time for expected LLJ emissions at 4.5 hr after sunrise, with sunrise calculated separately for each emitted plume based on location and time of year. In practice, plumes may only be observable to the plume tracking system described in section 2 a short while after emission, and some will precede the expected peak time. Hence, a time window of 0600 to 1600 UTC is specified in which LLJ emission is possible, although plumes very late or early in this period will score poorly in this timing criterion. Outside of these hours, emissions are assumed not to be associated with LLJ activity. Although sporadic turbulence overnight is possible due to wind shear, lidar profiles from the Fennec Campaign (Allen & Washington, 2014) provide little evidence to suggest these drive overnight emission, as this process will actually tend to erode the LLJ too gradually for it to obtain erosive potential (Knippertz & Todd, 2012).

3.4. Deep Convection Association

A second predictor of a plume's emission mechanism is its association with deep convection, as Saharan CPOs are a result of convective downdrafts.

Here, the distance of the centroid of a plume at the point of its emission to the nearest pixel with a BT10.8- μm value under 270 K is used as a proxy for its association with deep convection. Centroids throughout this paper are calculated from the mean of all latitude and longitude values associated with pixels comprising a feature. The choice of BT threshold follows the approach of Lavaysse et al. (2009) and Ashpole and Washington (2013b) for identifying deep convective cloud features. Although LLJ emission in close proximity to deep convection is a possibility, model estimates of dust emission under cloud suggest a small fraction of LLJ associated uplift occurs under cloud (Heinold et al. (2013). Furthermore, dust emitted far (hundreds of kilometers) from deep convection is unlikely to be associated with CPOs except for the most vigorous, far-ranging cases. Plumes with a high distance to deep convection are therefore more likely to be identified in this scheme as LLJ related.

3.5. Geometry

In section 3.1, it was shown that emission events associated with CPOs exhibit typical characteristics of an advancing wall, while LLJ-driven plumes behave more as streaks. The streak-like geometry of LLJ plumes is particularly clear when all pixels across their lifetime are considered (Figure 7b) and can be compared to the bow-like shape of a CPO event (Figure 7a).

To quantify this geometric distinction, two variables are required: the direction in which the plume is traveling and its orientation. Plume direction is calculated by taking the angle between the plume's centroid

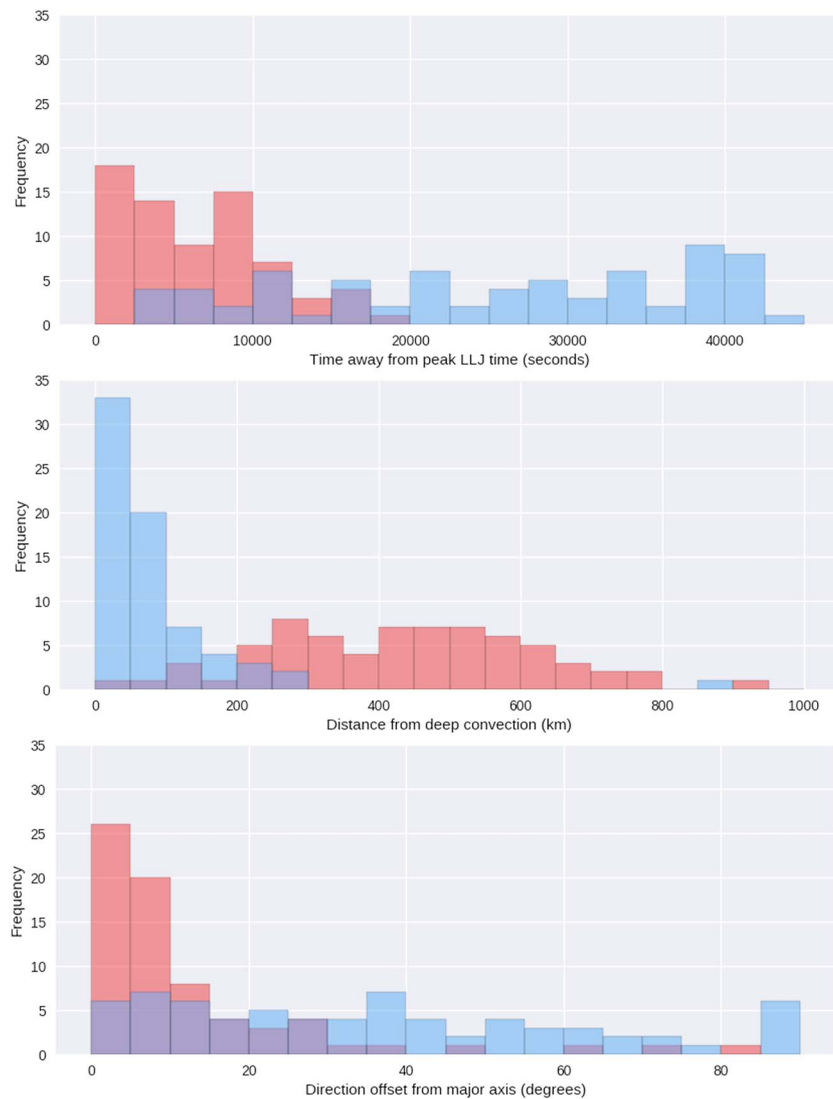


Figure 9. Distribution of values of predictors used for multiple logistic model of plume low-level jet (LLJ) probability, as calculated for manually identified LLJs (red) and cold pool outflows (blue) from 2010, including (a) the time in seconds away from peak expected LLJ emission time, (b) the distance to the nearest deep convection in kilometers, and (c) the offset angle (the maximum being perpendicular) of the plume's direction of propagation from its major axis (orientation).

during its first and last time steps. Orientation is calculated by taking the union of all pixels across the plume's lifetime (all activated pixels over all time steps in Figure 7) and calculating the first eigenvector from a principal component analysis of these pixels (on a longitude-latitude axis). The difference between the plume direction and orientation may then vary from 0 to 90°. Lower values indicate a plume propagating along its orientation (more LLJ-like), while higher values suggest propagation perpendicular to orientation (more CPO-like). Here, this quantity is termed the “axis offset” of a plume.

Unlike emission timing and association with deep convection, calculation of this quantity relies on obtaining a stable estimate of variables from a plume's total lifetime. For this reason, plumes with a very short duration are not reliable. Hence, in this paper a probability value is only calculated for plumes with a duration greater than or equal to 2 hr. Axis offset values tend to vary significantly within the first few time steps of a plume's lifetime (Figure 8). After 2 hr, however, the change in axis offset from one time step to the next does not exceed 10° on average. Geometries calculated for plumes with this duration are considered to be representative of the plume's true emission mechanism.

3.6. Regression Model

A single probability is assigned to each plume, using a multiple logistic regression model to account for the three predictive characteristics. Logistic regression is used here as the dependent variable is a binary classification. It is assumed that a plume adopts one classification to the exclusion of the other; hence, a plume cannot be both a highly probable LLJ and highly probable CPO. As a result, this probability varies from 0 (high confidence CPO) to 1 (high confidence LLJ) since the conditions bound up with the CPOs and LLJs are mutually exclusive. Each of the three predictive characteristics are therefore selected such that LLJs and CPOs produce opposite signals, as shown in sections 3.3 to 3.5.

The final assigned value should be interpreted as the probability that a manual observer would identify the plume as being LLJ driven, assuming all events are driven by either LLJs or CPOs (see section 3.7 for other mechanisms). This value is calculated as

$$P_L = \left(\frac{1}{1 + \exp(-\beta_0 - \beta_1 X_1 - \beta_2 X_2 - \beta_3 X_3)} \right), \quad (1)$$

where P_L is the probability of a given plume being an LLJ under the identification scheme, X_i is the value of predictors variables 1–3 (timing of emission, deep convective association, and geometry), and β_i is the corresponding regression parameter. As some events cannot be unambiguously categorized as LLJ or CPO driven, this system represents these with low probabilities (in this case values close to 0.5, indicating no strong preference either way).

Given a probability of being either LLJ or CPO driven, a plume can be categorized based on a user-defined threshold. Here, we identify LLJ dust as being plumes with an LLJ probability of 0.5 or over, while CPO dust is identified where a plume's LLJ probability is under 0.5.

With values of X_i available from quantified plume characteristics, corresponding values for β_i are needed to obtain a final probability value for a given plume. These are obtained by fitting the model to a set of “true” LLJ and CPO cases. As the goal of the probabilistic scheme is to replicate the manual observer automatically, this training data set is generated by manually identifying a series of clear cases from year 2010 only. In total, 141 events are categorized; in order to maintain comparable sample sizes, these are split almost evenly between LLJs (71) and CPOs (70). This is not, however, intended to represent the true partitioning of events.

For each predictor, a clear distinction between the distributions for manually identified LLJ and CPO events (Figure 9) demonstrates that the choice of criteria is appropriate. The majority of plumes manually identified as LLJs were found by the automated tracking system to have been emitted within 10,000 s (2.7 hr) of the peak expected time (Figure 9a). In the case of CPOs, a flatter distribution is found, with little evidence for a preference for emission at any particular time. The distance of a plume from deep convection at the point of its emission is a clear identifier of CPO events. While LLJ plumes are somewhat clustered around 200–400 km away from deep convection, the vast majority of plumes manually identified as CPOs are emitted within 200 km of the nearest identifiable convective cell (Figure 9b). The metric of geometry, offset of the plume from its major axis (orientation), is similarly distributed to the timing metric (Figure 9c). Plumes identified as LLJs align their propagation more closely with their orientation than do CPOs.

Solving the equation requires parameters (β_i) to be estimated from the training data set. A Bayesian approach is taken to fitting the model defined in equation (1). This means that rather than directly selecting the maximum likelihood estimate for the parameter values (β_i), a distribution (“posterior distribution”) of model parameters is obtained. To approximate the posterior distribution given the observed data, the No-U-Turn Sampler (Hoffman & Gelman, 2014) is used. This Bayesian approach in principle allows prior distributions to be specified and combined with the observed data to produce the posterior. In this paper, no prior distributions are specified (i.e., a uniform prior is used for each predictor), meaning there is little difference with the result that would be obtained using a maximum likelihood approach. With a posterior distribution of parameters, we obtain a corresponding distribution of probabilities from which the mean is calculated. Nonetheless, the adoption of a Bayesian approach means that priors could be incorporated into the methodology in future, for instance when better in situ observations of the morphology of LLJ and CPO dust plumes are available.

3.7. Other Emission Mechanisms

Our method focuses upon dust emission visible in satellite imagery. Emission mechanisms operating on a significantly smaller scale, such as dust devils, are therefore unlikely to be observable.

Table 1*Plume Emission Mechanisms Identified at Bordj-Badji Mokhtar (June 2011) as Identified by Allen et al. (2013)*

Date (a.m./p.m.)	Event type	Correct classification?
13/06/2011 a.m.	Cold pool advection	Yes
13/06/2011 p.m.	Cold pool emission	Yes
14/06/2011 a.m.	Cold pool advection	Yes
14/06/2011 a.m.	Low-level jet	No
14/06/2011 p.m.	Cold pool advection	Yes
15/06/2011 a.m.	Cold pool advection	No
16/06/2011 a.m.	Low-level jet	Yes
17/06/2011 a.m.	Cold pool advection	Yes
17/06/2011 p.m.	Cold pool emission	Yes
18/06/2011 a.m.	Cold pool emission	Yes
18/06/2011 a.m.	Low-level jet	No
19/06/2011 a.m.	Cold pool emission	Yes
19/06/2011 p.m.	Cold pool advection	Yes
21/06/2011 a.m.	Cold pool emission	Yes
21/06/2011 p.m.	Cold pool emission	Yes
22/06/2011 a.m.	Cold pool emission	Yes
22/06/2011 p.m.	Cold pool emission	Yes
23/06/2011 a.m.	Cold pool advection	Yes
24/06/2011 a.m.	Cold pool emission	Yes
24/06/2011 p.m.	Cold pool emission	Yes
25/06/2011 a.m.	Low-level jet	No
25/06/2011 p.m.	Cold pool emission	Yes
26/06/2011 a.m.	Low-level jet	Yes
27/06/2011 a.m.	Cold pool advection	No
29/06/2011 a.m.	Low-level jet	Yes
29/06/2011 p.m.	Low-level jet	Yes
30/06/2011 a.m.	Cold pool emission	Yes
30/06/2011 p.m.	Cold pool emission	Yes

Cold surges from maritime regions (Vizy & Cook, 2009) have been observed to drive gusty winds with emission potential close to the Mediterranean (Knippertz, 2008). No contribution to observed dust emission from such sources was found at Bordj-Badji Mokhtar during the Fennec Campaign (Allen et al., 2013), and, although these are uncommon and typically occur during winter (Wagner et al., 2016), events observed with this methodology are likely to be classified in this methodology as CPOs. To estimate the contribution of cold surges, imagery from June 2011 was analyzed. Three large plumes of dust emitted radially from the Mediterranean region in the northeast of the CWS were identified during this period, each of which was also associated with some degree of deep convection. Assuming these were cold surges, however, they accounted for 4.4% of the total dust pixels flagged for the month using the method in section 2, indicating a relatively minor contribution to total dust. Further work is required to distinguish cold pools generated by deep convection in the Atlas mountain regions and cold surges, driven for instance by lee cyclogenesis within the same region. As the bulk of dust emission during summer occurs further south in the Central Sahara than western Tunisia and northern Algeria near Mediterranean inflow regions, however (Ashpole & Washington, 2013b), these events are likely to have only a small impact upon the net partitioning of emission drivers.

4. Comparison With Manual Detection Methods and In Situ Observations

The availability of targeted observations from the Fennec Campaign in boreal summer allows the approaches used in this research to be validated in highly dust laden regions. We also validate the methodology against entirely manual identification based on SEVIRI imagery.

Table 2*Plume Emission Mechanisms (LLJs and CPOs only) Identified from Fennec Flights as Described by Ryder et al. (2015)*

Date (a.m./p.m.)	Event type	Correct classification?
17/06/2011 a.m.	Low-level jet	No
18/06/2011 a.m.	Low-level jet	Yes
21/06/2011 a.m.	Atlas cold pool	No
25/06/2011 a.m.	Low-level jet	Yes
27/06/2011 a.m.	Cold pool advection	No

Note. LLJ = low-level jet; CPO = cold pool outflow.

The automated dust plume classification approach compares well with events identified using in situ Fennec data but is limited by the sensitivity of SDFs to detect all emitted dust. Ryder et al. (2015), and Allen et al. (2013) catalog several LLJ and CPO events distinguished using a variety of land-based and airborne instrumentation (Tables 1 and 2). In total, 25 of the 33 (76%) events were both identified as dust and correctly classified. Two cases of incorrect classification were found, in both instances with a probability value indicating high uncertainty. Each remaining missed event is either obscured by existing dust emission or undetected by the automated dust detection scheme due to insensitivity or the inability to observe dust under cloud. Many of the LLJ dust events observed at Bordj-Badji Mokhtar are undetectable in SEVIRI using either manual or automated methods, possibly due to the presence of a surface temperature inversion or LLJ-generated dust not getting injected high enough to be distinguished with SEVIRI (Allen et al., 2013). Very short-lived plumes are not within the scope of this paper, as probabilities are only calculated for plumes with a minimum duration of 2 hr. Analysis of SEVIRI here is therefore limited to large plumes, which can be resolved and which have the vertical extent and/or duration to be distinguished from the desert surface. LLJs may, therefore, be a dominant driver of small-scale uplift, which does not fulfill these conditions.

Automatically, classified plumes are also compared with an entirely manual approach (as described in section 3.1). Using imagery from 2011, 65 of the clearest events have been identified as being either cold pool or LLJ driven. Of these, 57 were correctly identified using the automated method (87.7%). To examine the added value of this, it has been compared with an approach based purely on the timing of events; the accuracy of this method can be maximized at 76.9% if plumes are always identified as LLJs when emitted between the hours of 0600 and 1500 UTC (a more conservative cutoff of 1600 UTC is used in this paper as



Figure 10. Total yearly counts of pixels classified as belonging to cold pool outflow (blue)-driven and low-level jet (red)-driven dust events.

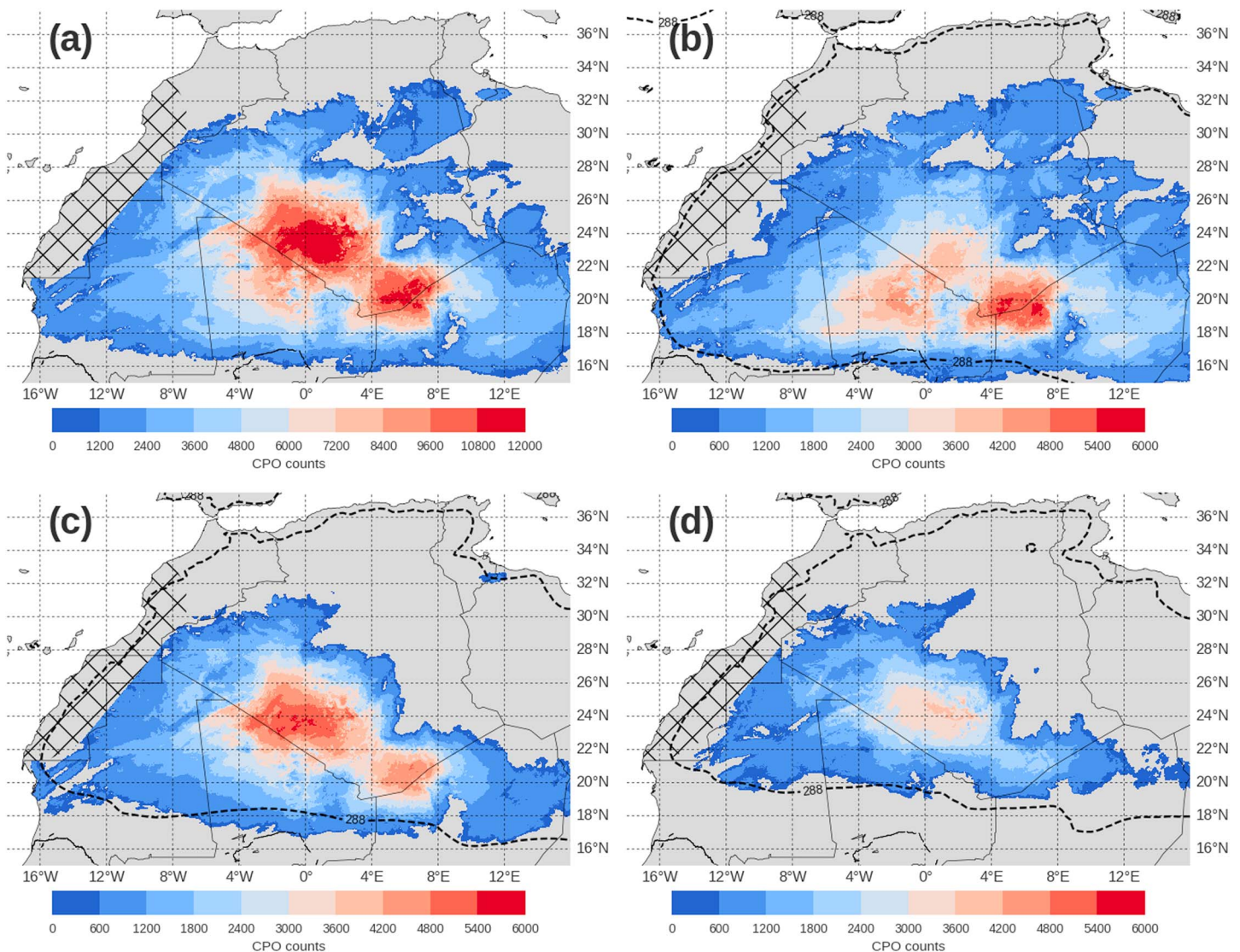


Figure 11. Total counts of pixels classified as belonging to cold pool outflow (CPO) events across the total lifetime of all plumes tracked from 2004 to 2017. The total for June–August is shown in (a), along with June (b), July (c), and August (d). The western region of the central and western Sahara along the coast of the Atlantic is masked (hatched area) following Ashpole and Washington (2013b), as this region is prone to false detections due to incursions of marine stratocumulus. Dashed black contour indicates the mean position of the 288-K, 10-m dew point temperature line from ERA5 for each constituent month (same period).

late-emitted LLJ plumes are occasionally found). The automated identification scheme in this research is therefore an improvement upon one based purely on the timing of emitted events.

5. Climatology of Emission Mechanisms

Having assigned probabilities to each plume of being associated with either an LLJ or CPO, in this section probabilities across the entire sampling period of June–August 2004–2017 are aggregated to build a climatology of dust-emitting LLJ and CPO events. This is achieved by identifying events with a probability of more than 0.5 as an LLJ and those with less than 0.5 as a CPO.

We analyze the contribution of each mechanism to the total SDF pixels across the sampling period to investigate their respective roles in Saharan emission although we recognize that this encapsulates both emission and transport processes (Ashpole & Washington, 2012); no information on dust optical depth is provided by SDFs, so highly dispersed aged plumes appear the same as freshly emitted ones. Nevertheless, the dust tracking scheme used in this work allows new plumes to be distinguished from aged ones, meaning plume activity at the point of emission can be studied.

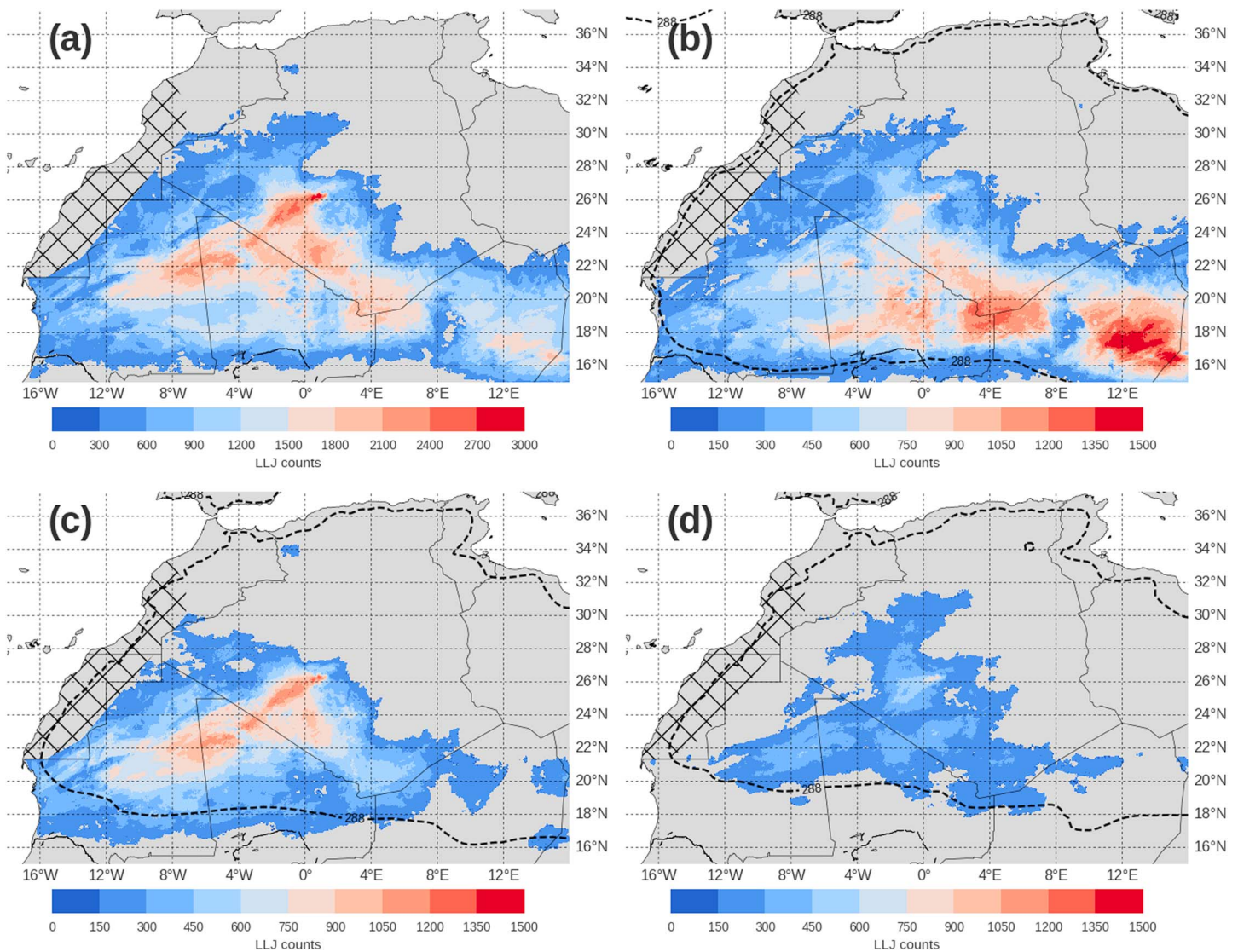


Figure 12. Total counts of pixels classified as belonging to low-level jet (LLJ) events across the total lifetime of all plumes tracked from 2004 to 2017. The total for June–August is shown in (a), along with June (b), July (c), and August (d). The western region of the central and western Sahara along the coast of the Atlantic is masked (hatched area) following Ashpole and Washington (2013b), as this region is prone to false detections due to incursions of marine stratocumulus. Dashed black contour indicates the mean position of the 288-K, 10-m dew point temperature line from ERA5 for each constituent month (same period).

Dust is associated above all with CPOs, accounting for 81.6% of the total pixels. The dominance of CPO dust is consistent in each year of the analysis (Figure 10), although the partitioning varies between 94% CPO in 2017 and 60% in 2012. Although the bulk of dust present over the CWS during summer is invariably CPO associated, the dustiest years are not necessarily those with the most CPO activity.

The largest concentrations of CPO-driven dust are found in a dipole pattern (Figure 11a) highly reminiscent of the distribution found by Ashpole and Washington (2012). One of these hot spots runs along the Mali–Algeria border, from 22° N to 26° N. While monsoon surges far north of the peak WAM rain zone are a known phenomenon (Lavaysse et al., 2011; Parker et al., 2005), the existence of this dust maximum suggests that northward moisture transport around the southeastern flank of the Saharan heat low is directly linked to dust-emitting cold pool activity in remote Saharan dust sources, as suggested by Garcia-Carreras et al. (2013) and Engelstaedter et al. (2015). A second (but closely linked) contributor to these northern hot spots is likely to be recycled cold pools, which have been observed propagating as far north as the foothills of the Atlas mountains (north of 28° N; Trzeciak et al., 2017). Although cold pool emission is significant

around the northern and southern fringes of the Sahara (Marshall et al., 2011), it also extends far into the central Sahara. The second region in the dipole, observed in the southeast around the Mali-Niger-Algeria triple point (19° N, 5° E), is coincident with a hot spot of orographic convection (Chaboureaud et al., 2016; Redl et al., 2015) and significant dust availability from a large region of ephemeral fluvial systems draining the Aïr and Hoggar ranges (Bou Karam et al., 2008).

Seasonal displacement of the CPO signal is particularly pronounced around the triple point region (Figures 11b and 11d). Ashpole and Washington (2013a) found that the early season dust maximum around the Mali-Niger-Algeria triple point migrates northwestward along the Mali-Algerian border as the summer progresses. Figures 11b and 11c indicate that this signal is dominated by the CPO dust response, lending credence to the importance of monsoon dynamics in this transition. A particularly significant component of these dynamics is the June onset of the WAM, during which accumulated convective inhibition, maintained in part by the dry northeasterly Harmattan, is broken and the rain band shifts north (Sultan & Janicot, 2003). While preonset monsoon surges advect considerable moisture into the central Sahara on weekly time scales (Couvreur et al., 2010), this onset coincides with the northward jump of cold pool emitted dust. Deep convective cloud cover increases considerably over these dust-emitting regions in July, reaching its maximum in August (Figures 13a–13c). The extension of deep convection north toward the border of Mali and Algeria during July (Figure 13b) coincides with the development of the CPO hot spot along this border region observed in Figure 11c. The evolution of this northward extension in monsoonal convection over Mali is likely, therefore, to be a major driver behind CPO-driven dust emissions in the remote Sahara north of 22° N.

LLJ-related dust (Figure 12) is lower in quantity (note the difference in the scale between Figures 11 and 12) and more geographically confined. A particular streak of high LLJ-driven dust emission is observed downstream (southwest) of the highly active Tidihelt Depression in central Algeria (26–27° N, 1° E), pointing to the existence of a distinct alley of LLJ activity between the Hoggar (22° N, 5° E) and Atlas (30° N, –4° E) mountains, in which CWS jet-driven dust peaks in boreal summer. As shown from the Fennec Campaign in 2011, dust-emitting LLJs are also active close to the dust source maximum further south along the southwestern Algerian border (Allen & Washington, 2014).

Similar to CPOs, a south-north propagation is evident in the intraseasonal development of LLJ dust (Figures 12b–12d). Dust in June is observed in the southeast of the domain around 17° N, 13° E in Niger south of the Ténéré Desert and west of Lake Chad, but this activity is absent in July and August. LLJ dust is also observed further north in June than in later months, with a band of emission aligned through the Grand Erg Occidental north of 27° N. The highest counts of activations within the Tidihelt Depression region occur during July, with LLJ activity dropping off considerably in August. A likely contributor to the development of this July maximum is the summertime evolution of the Saharan heat low (Figures 13d–13f). Whereas in June the low is centered over southern Algeria (Figure 13d), it extends northwestward during July, setting up a major pressure gradient region over central Algeria. This is evident in low-level wind fields (Figures 13g–13i), where a hot spot of surface wind speed develops around 27° N, 4° E in July, having been absent during June, reducing in August. Coincident with the Tidihelt region, this is the most likely driver behind the midsummer peak in the LLJ alley observed in Figure 12c. A weakening in the SHL in August may be responsible for the decline in dustiness for this month. Although Figure 13i suggests the effect upon surface winds is minor, the threshold-driven nature of dust emissions may be highly sensitive to the reduction in LLJ strength as a result of the gentler pressure gradient.

An interesting feature of the results is that although deep convective cloud reaches its maximum during August, this is the month when both CPO and LLJ dust totals actually drop off significantly. Enhanced cloud cover and water vapor over southern regions may explain some of this reduction in LLJ and CPO activity over monsoon regions in August. For instance, a comparison of SEVIRI dust source mapping with CALIOP observations suggests the southern Sahara and Sahelian sectors may be underobserved due to water vapor presence (Todd & Cavazos-Guerra, 2016). Multiple lines of evidence support a decline in overall dustiness during August, however. Aerosol Robotic Network 500-nm AOD observations from Tamanrasset for 2007, 2008, and 2011–2016 show a decline from a mean value of 0.52 in June to 0.43 in July and 0.36 in August. It is also suggested by a significant drop in August Aerosol Index over the CWS measured with the Total Ozone Mapping Spectrometer (TOMS AI) calculated from 1980 to 1992 (Engelstaedter et al., 2006) as well as MODIS DeepBlue aerosol optical thickness measured from 2006 to 2009 (Schepanski et al., 2012).

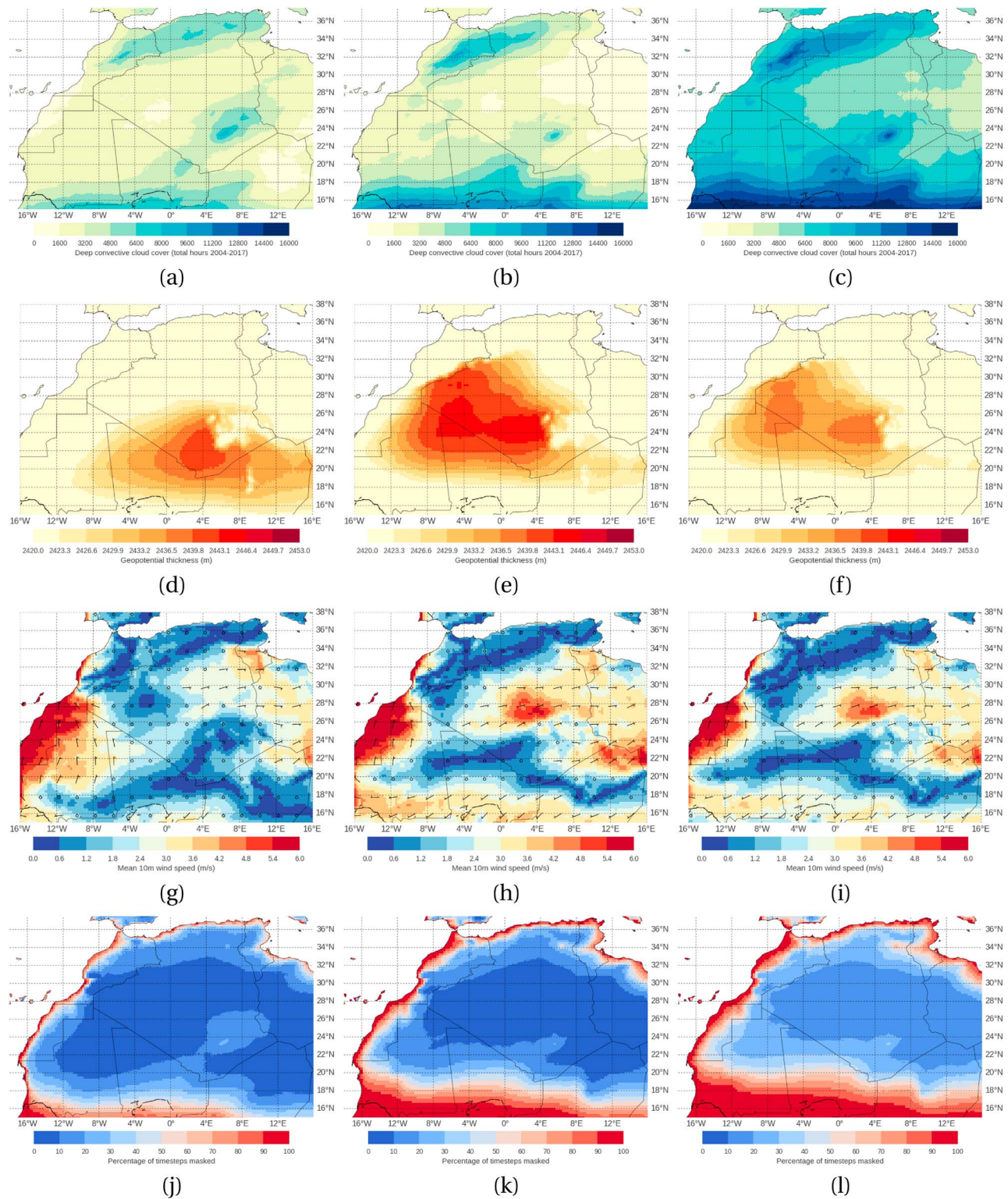


Figure 13. Controls upon observed cold pool outflow- and low-level jet-driven dust emission. Top row: total hours of deep convective cloud pixels in Spinning Enhanced Visible and Infrared Imager, defined where BT10.8 μm is under 230 K, for (a) June, (b) July, and (c) August. Second row: position of the Saharan heat low calculated as the mean 925- to 700-hPa geopotential thickness (meters); following Lavaysse et al., 2009) from ERA5 for (d) June, (e) July, and (f) August. Third row: mean ERA5 10-m wind speed for (g) June, (h) July, and (i) August. Fourth row: the percentage of time steps from 2004 to 2017 classified as masked (i.e., not visible for dust tracking) for (j) June, (k) July, and (l) August.

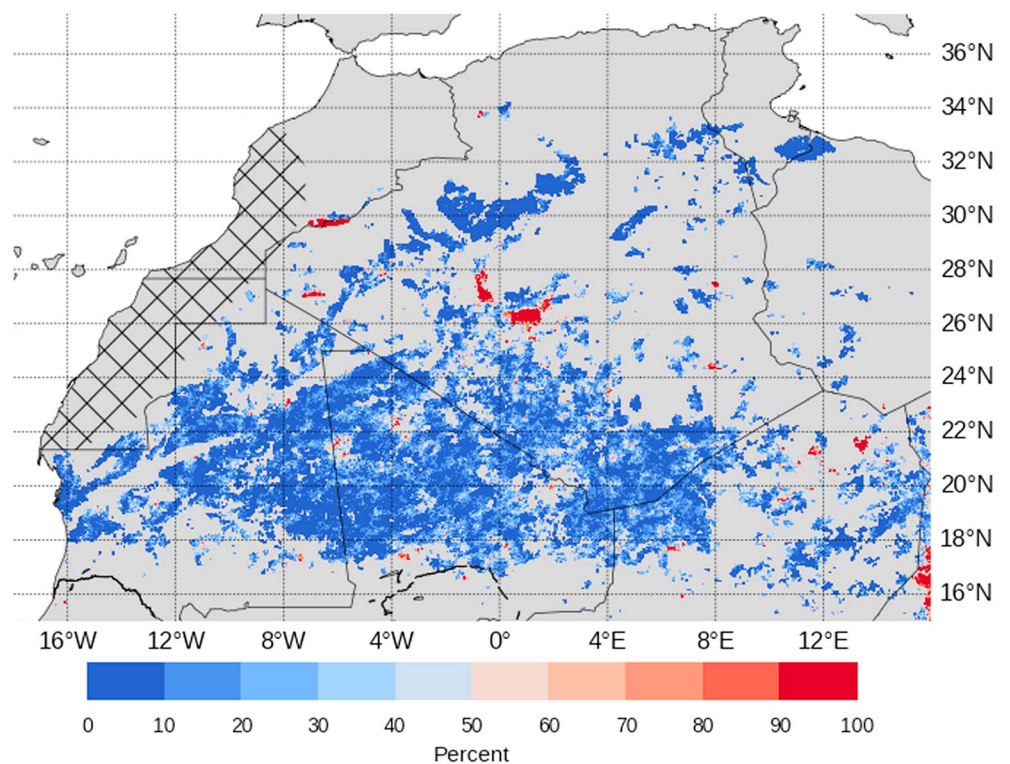


Figure 14. Percentage of emission pixels classified as being low-level jet driven for June, July, and August 2004–2017. Each pixel of a plume during the first four time steps of its life cycle is identified as an emission pixel. Regions with fewer than 10 emission pixels identified across the sampling period are masked out. The western region of the central and western Sahara along the coast of the Atlantic is masked (hatched area) following Ashpole and Washington (2013b), as this region is prone to false detections due to incursions of marine stratocumulus.

Although other data sets support this seasonal decline in observed dust, bias in SEVIRI may be contributing to the seasonality of the results presented here. As discussed in Ashpole and Washington (2012), dust cannot be observed under cloud and is obscured where high column water vapor is present (Banks et al., 2018; Brindley et al., 2012). Assuming seasonal variation in dust optical properties is negligible, water vapor and cloud are likely to be the main source of any bias when comparing early and late summer dust observations. To test this, we estimate a mask representing the percentage of time steps masked (i.e., invisible for detection of dust) across the domain for each of the 3 months (Figures 13j–13l). This is calculated by flagging a pixel as masked if it is either cloud-covered (BT10.8- μm value under 270 K) or located south of the intertropical discontinuity (ITD), using the ERA5 288-K dew point temperature contour. The ITD represents the confluence of the monsoonal and harmattan air masses in the central Sahara (Bou Karam et al., 2008; Engelstaedter & Washington, 2007) and is a region with a sharp increase of low-level atmospheric moisture content, with surface dew point temperature values between 287 and 289 K used previously as a proxy for the position of the ITD (Buckle, 1996; Eldridge, 1957; Marsham et al., 2008). In general, dust is obscured south of the climatological location of this boundary; this is demonstrated in Figures 11 and 12 by marking the mean seasonal position of the ITD. The analysis is applied to hourly data to match with the resolution of the ERA5 reanalysis. Maps of CPO and LLJ dust adjusted for masking effects (not shown) do not differ significantly from the results presented in Figures 11 and 12. Our unadjusted results show a 59% (75%) drop in CPO (LLJ) dust pixels between June and August, whereas adjusted results show a 53% (69%) drop. Hence, while biases in SEVIRI do play a small role in reducing visibility of dust during the peak of the monsoon, they are unlikely to be the driving factor behind the seasonality of the results presented here.

As the decline in dustiness during August is therefore likely to be genuine, questions remain as to why dust would decrease even as deep convective activity grows. One possible explanation is a decline in dust transport, for instance due to a weaker SHL (Figure 13f), but results from Ashpole and Washington (2013b) indicate that emissions also drop in this month. Assuming erodibility is constant, enhanced convective activity

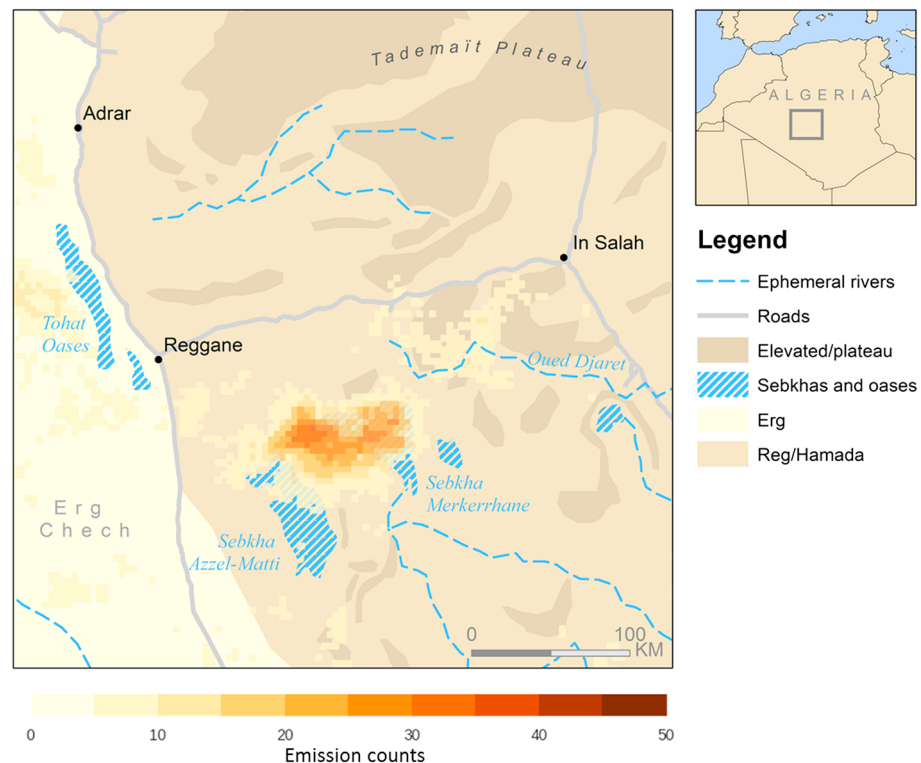


Figure 15. Map of the Tidihelt region identified as both a major dust source and low-level jet hot spot. Dust source activation totals from Figure 4 are overlain in shades of orange. Features of interest are symbolized as shown in the key. Region location within Algeria is shown in the top right.

may not necessarily correspond to increased generation of outflows. This will be tested in a subsequent paper, which focuses more directly upon the occurrence of these outflow boundaries.

Next we analyze the percentage of emission events driven by each mechanism in order to link CPO and LLJ activity to individual source regions. A pixel associated with a plume in the first time step of its life cycle is designated as an emission pixel. No information about plume transport is obtained from this metric, but it affords a more faithful description of the geographical distribution of the emission processes themselves.

Overall, 87.5% of emission pixels are associated with CPOs. The preference for CPO emission events is widely distributed across the peak CWS emission regions (Figure 14). Of the dust sources shown in Figure 4, the majority are dominated by CPO emissions, including around the Mali-Niger-Algeria triple point. In this region, marked as (f) in Figure 16, plumes tend to propagate in a westward or northwestward direction, bounded by the Air Mountains to the west. The area labeled under (d) as the Tamanrasset region in Figure 16 has a more even distribution of plume directions, indicating the hot spot of cold pool-generated dust present in July in Figure 11c is associated with locally generated cold pools as well as those propagating from the ITD zone in the south. Almost all emissions in Mali are associated with CPOs, with a small contribution from LLJs near the Taoudenni basin (22° N, 4° W), long identified as a dust source of global significance (Washington et al., 2003). Probabilities for regions with high CPO activity are typically dominated by values of zero, with 80% of CPO pixels having been assigned this value. This signifies that in most instances, plumes identified as CPOs were given that classification simply because they occurred at a time of day when only CPOs are considered possible under the automated system (section 3.3).

Unlike the widespread emissions from CPOs, LLJ emission is dominated by activity within the low lying Tidihelt region of central Algeria (Figure 14, and shown in Figure 15). This indicates that although CPOs are a dominant emission mechanism across the CWS during boreal summer, the single most frequently activated source at this time of year is almost entirely driven by LLJs. Within the broad Harmattan channel between the Atlas and Hoggar ranges, the Tidihelt region is approximately 200 km southeast of the windiest observed region in Algeria, Adrar (28° N, 0° E; Chellali et al., 2011). The numerous endorheic basins (in

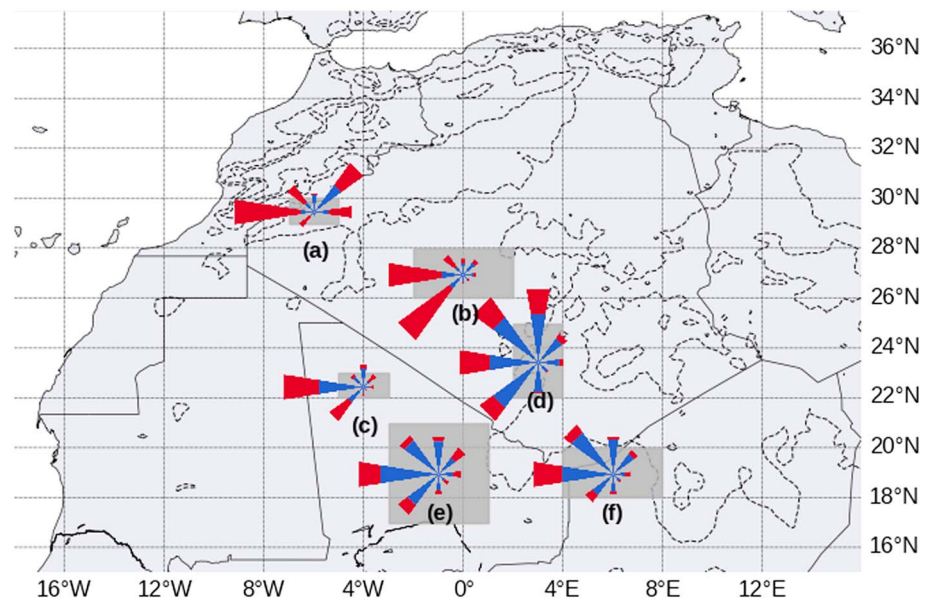


Figure 16. Preferred propagation directions of plumes at selected dust sources. Wind rose segments indicate the percentage frequency of a direction in which plumes are traveling (i.e., a segment pointing west indicates plumes traveling west). The red component of the segment indicates the proportion of events associated with low-level jets, while the blue represents cold pool outflow events. Propagation direction is calculated from the difference between the centroid of the plume in its first time step and its last. Gray boxes represent the region from which plumes were sampled for each wind rose. Sample regions include (a) Lake Iriki, (b) Tidihelt Depression, (c) Taoudenni region, (d) Tamanrasset region, (e) Adrar des Ifoghas region, and (f) Valle de l'Azaouagh. Dashed black contours indicate orography at 500-m intervals.

particular Sebkha Mekerrhane and Sebkha Azzel-Matti) with large saline deposits and erodible material lie in the lowland plain near In Salah at the opening between the Tademaït Plateau and Mouydir Mountains, which drain into the Tidihelt below (Hughes, 1992). Along with the Tohat Oases to the northwest, these are the last major emission hot spots before the desert opens out into Erg Chech to the west. The idealized map of regions of likely LLJ enhancement derived by Heinold et al. (2015) suggests that the surface roughness in this region may be particularly conducive to ageostrophic winds and hence high-amplitude inertial oscillation. Although plumes identified as CPOs are active, dust source activation in the Tidihelt is almost entirely associated with LLJs propagating southwestward in the dry Harmattan (Figure 16). The lack of further LLJ hot spots to the southwest also suggests that the LLJ signal many hundreds of kilometers downstream of the Tidihelt observed in Figure 12a is largely a result of transported events rather than fresh emission. Tidihelt LLJs are therefore highly effective at contributing to long-range transport by the Harmattan, which is important for the production of a Saharan air layer over the Atlantic (Bou Karam et al., 2008; Schwendike et al., 2016). A further study will explore drivers of LLJ activity within the Tidihelt region in more detail.

An additional LLJ hot spot is found along the border of Mali and Morocco, in the dust source identified by Ashpole and Washington (2013b) as Lake Iriki (30° N, 6° W). This is a much less active dust source than the Tidihelt (Figure 4), but the preferred direction for plumes here is westward (Figure 16), indicating a possible local constraint on plume propagation. Other sources with greater CPO activity, for example, source (d) in Figure 16, have a more even distribution of preferred plume directions, except that plumes seldom travel southeastward. Although LLJ hot spots have preferred directions, LLJs on the whole are not unique to one particular wind regime; as found in Allen et al. (2013), they may be embedded in both dry northeasterly and moister southerly or southwesterly flow.

The results shown in this section demonstrate that while CPO-emitted dust is widespread across the central Saharan dust sources, LLJs dominate in a small selection of hot spots. Most of the observed pattern of summertime dust as observed using SEVIRI is not, therefore, attributable to LLJ activity. Nevertheless, as suggested in section 4, LLJs may be important for short-lived plumes that go undetected by the SDF scheme, and they play a very large role in one of the desert's single most frequently activated source regions. Accurate representation of LLJ emission of dust therefore relies upon an understanding of local surface and

orographic conditions and how they influence inertial oscillation. Although LLJs are typically represented in most wind fields used to drive offline dust models, a more meticulous analysis of the erosive conditions in a small set of highly concentrated LLJ-dominated source regions is needed. By contrast, CPOs are not explicitly simulated in models and represented only via convective parameterization schemes and therefore contribute to moisture transport errors (Garcia-Carreras et al., 2013). The overwhelming significance of CPO dust found in this analysis is in agreement with in situ observations (Allen et al., 2013) and confirms the strong link between WAM dynamics and uplift of dust during the boreal summer emission maximum.

6. Summary and Conclusions

Automatically tracked dust plumes emitted during boreal summer for the period 2004–2017 have been probabilistically categorized as either LLJ or CPO emissions. To support this approach, an improved method to track dust with SDFs has been developed. The new dust tracking scheme is better at accurately detecting dust emission time, and fewer aged plumes are incorrectly classified as freshly emitted due to flickering or weak nocturnal detection. Three quantifiable characteristics were identified, which can be used to classify plumes: the timing of emission, the distance from deep convection at the point of emission, and the orientation relative to the direction of propagation. Combining each of these into a multiple regression model yields an accurate method of partitioning satellite-observed dust by mechanism. This classification scheme improves upon approaches based entirely upon the timing of plumes. Short-lived plumes from LLJs are likely to be underestimated, however, as the thresholding approach relies upon plumes being lofted high enough to be thermally distinct from the surface.

CPO activity is found to dominate the dust signal overall, accounting for 81.6% of the dust-flagged pixels. This may be a slight overestimate, however, as a manual analysis of a sample of the data revealed that 4.4% of dust pixels were associated with possible cold surge events, and these are likely to have been classified as CPOs by the automated system. Dust from cold pools is organized into a dipole pattern, which evolves from a preference for the triple point of Mali-Niger-Algeria in June toward higher activity further north along the Algerian border with Mali later in the season. A similar northward shift is observed for LLJs. However, diminished activity along the fringe of the Sahel later during the monsoon season is likely also a result of bias introduced by advancing cloud from the onset of the WAM. LLJ dust is organized along a northeasterly channel originating between the Hoggar and Atlas ranges. Partitioning of mechanisms at the point of emission reveals that while the bulk of emission from sources along the foothills of the Hoggar range, around Adrar des Ifoghas, and within northern Niger are due to cold pool activity, LLJs are extremely important in the Tidihelt Depression of central Algeria. This indicates that while cold pools have the widest reach in activation of the CWS, LLJs are responsible for one of the single most frequently activated source regions.

The data set derived in this study for the central Sahara is a useful means of linking variability in Saharan dust back to atmospheric controls of the emission processes at source. Furthermore, its application to a very large sample of satellite imagery offers a robust climatological perspective, which confirms the central role of deep convective processes for emissions in the world's largest boreal summer dust source. These findings underscore the need for dust models to be driven with meteorological data sets capable of resolving both deep convection and cold pools. Most current generation reanalysis products fall short of this, however. It follows that an improved understanding of the controls on CPO and LLJ variability through summer will be essential as the next generation of driving data sets are developed and validated.

References

- Ackerman, S. A. (1997). Remote sensing aerosols using satellite infrared observations. *Journal of Geophysical Research*, 102, 17,069–17,079.
- Allen, C. J., Washington, R., & Saci, A. (2015). Dust detection from ground-based observations in the summer global dust maximum: Results from Fennec 2011 and 2012 and implications for modeling and field observations. *Journal of Geophysical Research: Atmospheres*, 120, 897–916. <https://doi.org/10.1002/2014jd022655>
- Allen, C. J., & Washington, R. (2014). The low-level jet dust emission mechanism in the central Sahara: Observations from Bordj-Badji Mokhtar during the June 2011 Fennec Intensive Observation Period. *Journal of Geophysical Research: Atmospheres*, 119, 2990–3015. <https://doi.org/10.1002/2013jd020594>
- Allen, C. J., Washington, R., & Engelstaedter, S. (2013). Dust emission and transport mechanisms in the central Sahara: Fennec ground-based observations from Bordj-Badji Mokhtar June 2011. *Journal of Geophysical Research: Atmospheres*, 118, 6212–6232. <https://doi.org/10.1002/jgrd.50534>

Acknowledgments

MSG SEVIRI data are available online from the EUMETSAT Data Centre (<https://www.eumetsat.int/website/home/Data/DataDelivery/EUMETSATDataCentre/>). AWS data were obtained during the Natural Environment Research Council (NERC) Fennec field campaign (Grant NE/G017166/1), with thanks to those who installed and maintained the instrumentation, including the Algerian and Mauritanian Meteorological Offices. Fennec data are available from the Centre for Environmental Data Analysis (<http://archive.ceda.ac.uk/>). ERA5 data are maintained by the European Centre for Medium-Range Weather Forecasts and is available from the Copernicus Climate Change Service (<https://climate.copernicus.eu/climate-reanalysis>). T. C. H. is funded through the NERC doctoral training partnership (NE/L002612/1). R. W. was partly supported by the NERC-Department for International Development (DFID)-funded Improving Model Processes for African Climate (IMPALA) project (Grant NE/M017206/1), as part of the Future Climate for Africa (FCFA) program (<http://futureclimateafrica.org/project/impala/>). We would like to thank Ian Ashpole for his assistance with the use of SEVIRI dust flags, as well as three anonymous reviewers for their insightful comments.

- Ashpole, I., & Washington, R. (2012). An automated dust detection using SEVIRI: A multiyear climatology of summertime dustiness in the central and western Sahara. *Journal of Geophysical Research*, 117, D08202. <https://doi.org/10.1029/2011JD016845>
- Ashpole, I., & Washington, R. (2013a). Intraseasonal variability and atmospheric controls on daily dust occurrence frequency over the central and western Sahara during the boreal summer. *Journal of Geophysical Research: Atmospheres*, 118, 12,915–12,926. <https://doi.org/10.1002/2013JD020267>
- Ashpole, I., & Washington, R. (2013b). A new high-resolution central and western Saharan summertime dust source map from automated satellite dust plume tracking. *Journal of Geophysical Research: Atmospheres*, 118, 6981–6995. <https://doi.org/10.1002/jgrd.50554>
- Bagnold, R. A. (1941). The physics of blown sand and desert dunes, Methuen.
- Bain, C. L., Parker, D. J., Taylor, C. M., Kergoat, L., & Guichard, F. (2010). Observations of the nocturnal boundary layer associated with the West African monsoon. *Monthly Weather Review*, 138, 3142–3156.
- Banks, J. R., Schepanski, K., Heinold, B., Hünnerbein, A., & Brindley, H. E. (2018). The influence of dust optical properties on the colour of simulated MSG-SEVIRI Desert Dust infrared imagery. *Atmospheric Chemistry and Physics*, 18(13), 9681–9703.
- Blackadar, A. (1957). Boundary layer wind maxima and their significance for the growth of nocturnal inversions. *Bulletin of the American Meteorological Society*, 38(5), 283–290.
- Bou Karam, D., Flamant, C., Knippertz, P., Reitebuch, O., Pelon, J., Chong, M., & Dabas, A. (2008). Dust emissions over the Sahel associated with the West African monsoon intertropical discontinuity region: A representative case-study. *Quarterly Journal of the Royal Meteorological Society*, 134(632), 621–634.
- Boucher, O., Randall, D., Artaxo, P., Bretherton, C., Feingold, G., Forster, P., et al. (2013). Clouds and aerosols, *Climate change 2013: The physical science basis. Contribution of Working Group I to the Fifth Assessment Report of the Intergovernmental Panel on Climate Change* (pp. 571–657). Cambridge: Cambridge University Press.
- Brindley, H., Knippertz, P., Ryder, C., & Ashpole, I. (2012). A critical evaluation of the ability of the Spinning Enhanced Visible and Infrared Imager (SEVIRI) thermal infrared red-green-blue rendering to identify dust events: Theoretical analysis. *Journal of Geophysical Research*, 117, D07201. <https://doi.org/10.1029/2011jd017326>
- Buckle, C. (1996). Weather and climate in Africa. Longman.
- Chaboureaud, J.-P., Flamant, C., Dauhut, T., Kocha, C., Lafore, J.-P., Lavaysse, C., et al. (2016). Fennec dust forecast intercomparison over the Sahara in June 2011. *Atmospheric Chemistry and Physics Discussions*, 16, 6977–6995.
- Chellali, F., Khellaf, A., Belouchrani, A., & Recioui, A. (2011). A contribution in the actualization of wind map of Algeria. *Renewable and Sustainable Energy Reviews*, 15(2), 993–1002.
- Chelton, D. B., Freilich, M. H., & Esbensen, S. K. (2000). Satellite observations of the wind jets off the Pacific coast of Central America. Part I: Case studies and statistical characteristics. *Monthly Weather Review*, 128(7), 1993–2018.
- Choobari, O. A., Zawar-Reza, P., & Sturman, A. (2014). The global distribution of mineral dust and its impacts on the climate system: A review. *Atmospheric Research*, 138, 152–165.
- Couvreux, F., Guichard, F., Bock, O., Campistron, B., Lafore, J.-P., & Redelsperger, J.-L. (2010). Synoptic variability of the monsoon flux over West Africa prior to the onset. *Quarterly Journal of the Royal Meteorological Society*, 136(S1), 159–173.
- Cuevas, E., Gómez-Peláez, A., Rodríguez, S., Terradellas, E., Basart, S., García, R., et al. (2017). The pulsating nature of large-scale Saharan dust transport as a result of interplays between mid-latitude Rossby waves and the North African Dipole Intensity. *Atmospheric Environment*, 167, 586–602.
- Eldridge, R. (1957). A synoptic study of west african disturbance lines. *Quarterly Journal of the Royal Meteorological Society*, 83(357), 303–314.
- Emmel, C., Knippertz, P., & Schulz, O. (2010). Climatology of convective density currents in the southern foothills of the Atlas Mountains. *Journal of Geophysical Research*, 115, D11115. <https://doi.org/10.1029/2009jd012863>
- Engelstaedter, S., Tegen, I., & Washington, R. (2006). North African dust emissions and transport. *Earth-Science Reviews*, 79(1), 73–100.
- Engelstaedter, S., & Washington, R. (2007). Atmospheric controls on the annual cycle of North African dust. *Journal of Geophysical Research*, 112, D03103.
- Engelstaedter, S., Washington, R., Flamant, C., Parker, D. J., Allen, C., & Todd, M. (2015). The Saharan heat low and moisture transport pathways in the central Sahara: Multi-aircraft observations and Africa-LAM evaluation. *Journal of Geophysical Research: Atmospheres*, 120, 4417–4442. <https://doi.org/10.1002/2015jd023123>
- Evan, A. T., Flamant, C., Fiedler, S., & Doherty, O. (2014). An analysis of aeolian dust in climate models. *Geophysical Research Letters*, 41, 5996–6001.
- Fiedler, S., Knippertz, P., Woodward, S., Martin, G. M., Bellouin, N., Ross, A. N., et al. (2016). A process-based evaluation of dust-emitting winds in the CMIP5 simulation of HadGEM2-ES. *Climate Dynamics*, 46(3-4), 1107–1130.
- Fiedler, S., Schepanski, K., Heinold, B., Knippertz, P., & Tegen, I. (2013). Climatology of nocturnal low-level jets over North Africa and implications for modeling mineral dust emission. *Journal of Geophysical Research: Atmospheres*, 118, 6100–6121. <https://doi.org/10.1002/jgrd.50394>
- García-Carreras, L., Marsham, J., Parker, D., Bain, C., Milton, S., Saci, A., et al. (2013). The impact of convective cold pool outflows on model biases in the Sahara. *Geophysical Research Letters*, 40, 1647–1652. <https://doi.org/10.1002/grl.50239>
- Garreaud, R., & Muñoz, R. C. (2005). The low-level jet off the west coast of subtropical South America: Structure and variability. *Monthly Weather Review*, 133(8), 2246–2261.
- Ge, J. M., Liu, H., Huang, J., & Fu, Q. (2016). Desert nocturnal low-level jet: climatology and dust activity. *Atmospheric Chemistry and Physics*, 16(12), 7773–7783.
- Gentine, P., Garelli, A., Park, S.-B., Nie, J., Torri, G., & Kuang, Z. (2016). Role of surface heat fluxes underneath cold pools. *Geophysical research letters*, 43, 874–883. <https://doi.org/10.1002/2015gl067262>
- Heinold, B., Knippertz, P., & Beare, R. J. (2015). Idealized large-eddy simulations of nocturnal low-level jets over subtropical desert regions and implications for dust-generating winds. *Quarterly Journal of the Royal Meteorological Society*, 141(690), 1740–1752.
- Heinold, B., Knippertz, P., Marsham, J., Fiedler, S., Dixon, N., Schepanski, K., et al. (2013). The role of deep convection and nocturnal low-level jets for dust emission in summertime West Africa: Estimates from convection-permitting simulations. *Journal of Geophysical Research: Atmospheres*, 118, 4385–4400. <https://doi.org/10.1002/jgrd.50402>
- Hobby, M., Gascoyne, M., Marsham, J. H., Bart, M., Allen, C., Engelstaedter, S., et al. (2013). The Fennec automatic weather station (AWS) network: Monitoring the Saharan climate system. *Journal of Atmospheric and Oceanic Technology*, 30(4), 709–724.
- Hoffman, M. D., & Gelman, A. (2014). The No-U-turn sampler: Adaptively setting path lengths in Hamiltonian Monte Carlo. *Journal of Machine Learning Research*, 15(1), 1593–1623.
- Holben, B. N., Eck, T. F., Slutsker, I., Tanre, D., Buis, J., Setzer, A., et al. (1998). AERONET-A federated instrument network and data archive for aerosol characterization. *Remote Sensing of Environment*, 66(1), 1–16.

- Huang, Q., Marsham, J. H., Tian, W., Parker, D. J., & Garcia-Carreras, L. (2018). Large-eddy simulation of dust-uplift by a haboob density current. *Atmospheric Environment*, 179, 31–39.
- Hughes, R. H. (1992). A directory of African wetlands, IUCN.
- Huneus, N., Schulz, M., Balkanski, Y., Griesfeller, J., Prospero, M., Kinne, S., et al. (2011). Global dust model intercomparison in AeroCom phase I. *Atmospheric Chemistry and Physics*, 11, 7781–7816.
- Knippertz, P. (2008). Dust emissions in the West African heat trough—The role of the diurnal cycle and of extratropical disturbances. *Meteorologische Zeitschrift*, 17(5), 553–563.
- Knippertz, P., Deutscher, C., Kandler, K., Müller, T., Schulz, O., & Schütz, L. (2007). Dust mobilization due to density currents in the Atlas region: Observations from the Saharan Mineral Dust Experiment 2006 field campaign. *Journal of Geophysical Research*, 112, D21109. <https://doi.org/10.1029/2007jd008774>
- Knippertz, P., & Todd, M. C. (2010). The central west Saharan dust hot spot and its relation to African easterly waves and extratropical disturbances. *Journal of Geophysical Research*, 115, D12117. <https://doi.org/10.1029/2009JD012819>
- Knippertz, P., & Todd, M. C. (2012). Mineral dust aerosols over the Sahara: Meteorological controls on emission and transport and implications for modeling. *Reviews of Geophysics*, 50, RG1007. <https://doi.org/10.1029/2011RG000362>
- Koren, I., & Kaufman, Y. J. (2004). Direct wind measurements of Saharan dust events from Terra and Aqua satellites. *Geophysical Research Letters*, 31, L06122. <https://doi.org/10.1029/2003GL019338>
- Lavaysse, C., Chaboureaud, J.-P., & Flamant, C. (2011). Dust impact on the West African heat low in summertime. *Quarterly Journal of the Royal Meteorological Society*, 137(658), 1227–1240.
- Lavaysse, C., Flamant, C., Janicot, S., Parker, D., Lafore, J.-P., Sultan, B., & Pelon, J. (2009). Seasonal evolution of the West African heat low: a climatological perspective. *Climate Dynamics*, 33(2–3), 313–330.
- Lawson, T. (1971). Haboob structure at Khartoum. *Weather*, 26(3), 105–112.
- Lensky, I., & Rosenfeld, D. (2008). Clouds-aerosols-precipitation satellite analysis tool (CAPSAT). *Atmospheric Chemistry and Physics*, 8, 6739–6753.
- Mahajan, P., Mupmdar, V., & Ghanekar, S. (1989). Excitation of low-level jet as seen by GOES (IO) satellite off the Somali coast. *Advances in Atmospheric Sciences*, 6(4), 475–482.
- Marsham, J. H., Hobby, M., Allen, C., Banks, J., Bart, M., Brooks, B., et al. (2013). Meteorology and dust in the central Sahara: Observations from Fennec supersite-1 during the June 2011 Intensive Observation Period. *Journal of Geophysical Research: Atmospheres*, 118, 4069–4089. <https://doi.org/10.1002/jgrd.50211>
- Marsham, J. H., Knippertz, P., Dixon, N. S., Parker, D. J., & Lister, G. (2011). The importance of the representation of deep convection for modeled dust-generating winds over West Africa during summer. *Geophysical Research Letters*, 38, L16803. <https://doi.org/10.1029/2011gl048368>
- Marsham, J. H., Parker, D. J., Grams, C. M., Taylor, C. M., & Haywood, J. M. (2008). Uplift of Saharan dust south of the intertropical discontinuity. *Journal of Geophysical Research*, 113, D21102. <https://doi.org/10.1029/2008jd009844>
- Menut, L. (2008). Sensitivity of hourly saharan dust emissions to NCEP and ECMWF modeled wind speed. *Journal of Geophysical Research*, 113, D16201. <https://doi.org/10.1029/2007JD009522>
- Miller, S. D., Kuciauskas, A. P., Liu, M., Ji, Q., Reid, J. S., Breed, D. W., et al. (2008). Haboob dust storms of the southern Arabian Peninsula. *Journal of Geophysical Research*, 113, D01202. <https://doi.org/10.1029/2007JD008550>
- Parker, D., Burton, R., Diongue-Niang, A., Ellis, R., Felton, M., Taylor, C., & Tompkins, A. (2005). The diurnal cycle of the West African monsoon circulation. *Quarterly Journal of the Royal Meteorological Society*, 131(611), 2839–2860.
- Prospero, J. M., Ginoux, P., Torres, O., Nicholson, S. E., & Gill, T. E. (2002). Environmental characterization of global sources of atmospheric soil dust identified with the Nimbus 7 Total Ozone Mapping Spectrometer (TOMS) absorbing aerosol product. *Reviews of Geophysics*, 40(1), 1002. <https://doi.org/10.1029/2000RG000095>
- Provod, M., Marsham, J., Parker, D., & Birch, C. (2016). A characterization of cold pools in the West African Sahel. *Monthly Weather Review*, 144(5), 1923–1934.
- Ranjha, R., Svensson, G., Tjernström, M., & Semedo, A. (2013). Global distribution and seasonal variability of coastal low-level jets derived from ERA-Interim reanalysis. *Tellus A*, 65, 20412.
- Redl, R., Fink, A. H., & Knippertz, P. (2015). An objective detection method for convective cold pool events and its application to Northern Africa. *Monthly Weather Review*, 143(12), 5055–5072.
- Roberts, A., & Knippertz, P. (2012). Haboobs: Convectively generated dust storms in West Africa. *Weather*, 67(12), 311–316.
- Roberts, A., & Knippertz, P. (2014). The formation of a large summertime Saharan dust plume: Convective and synoptic-scale analysis. *Journal of Geophysical Research: Atmospheres*, 119, 1766–1785. <https://doi.org/10.1002/2013jd020667>
- Roberts, A. J., Marsham, J. H., Knippertz, P., Parker, D. J., Bart, M., Garcia-Carreras, L., et al. (2017). New Saharan wind observations reveal substantial biases in analysed dust-generating winds. *Atmospheric Science Letters*, 18(9), 366–372.
- Ross, A., Tompkins, A. M., & Parker, D. (2004). Simple models of the role of surface fluxes in convective cold pool evolution. *Journal of the atmospheric sciences*, 61(13), 1582–1595.
- Ryder, C., McQuaid, J., Flamant, C., Rosenberg, P., Washington, R., Highwood, E. J., et al. (2015). Advances in understanding mineral dust and boundary layer processes over the Sahara from Fennec aircraft observations. *Atmospheric Chemistry and Physics*, 15(14), 8479–8520.
- Schepanski, K., Tegen, I., Laurent, B., Heinold, B., & Macke, A. (2007). A new Saharan dust source activation frequency map derived from MSG-SEVIRI IR-channels. *Geophysical Research Letters*, 34, L18803. <https://doi.org/10.1029/2007gl030168>
- Schepanski, K., Tegen, I., & Macke, A. (2012). Comparison of satellite based observations of Saharan dust source areas. *Remote Sensing of Environment*, 123, 90–97.
- Schepanski, K., Tegen, I., Todd, M., Heinold, B., Bönisch, G., Laurent, B., & Macke, A. (2009). Meteorological processes forcing Saharan dust emission inferred from MSG-SEVIRI observations of subdaily dust source activation and numerical models. *Journal of Geophysical Research*, 114, D10201. <https://doi.org/10.1029/2008jd010325>
- Schwendike, J., Jones, S. C., Vogel, B., & Vogel, H. (2016). Mineral dust transport toward Hurricane Helene (2006). *Journal of Geophysical Research: Atmospheres*, 121, 5538–5566. <https://doi.org/10.1002/2015jd024708>
- Simpson, J. (1969). A comparison between laboratory and atmospheric density currents. *Quarterly Journal of the Royal Meteorological Society*, 95(406), 758–765.
- Soares, P. M., Cardoso, R. M., Semedo, Á., Chinista, M. J., & Ranjha, R. (2014). Climatology of the Iberia coastal low-level wind jet: Weather research forecasting model high-resolution results. *Tellus A*, 66, 22377.
- Sultan, B., & Janicot, S. (2003). The West African monsoon dynamics. Part II: The preonset and onset of the summer monsoon. *Journal of climate*, 16(21), 3407–3427.
- Sutton, L. (1925). Haboobs Haboobs. *Quarterly Journal of the Royal Meteorological Society*, 51(213), 25–30.

- Tegen, I., Schepanski, K., & Heinold, B. (2013). Comparing two years of saharan dust source activation obtained by regional modelling and satellite observations. *Atmospheric Chemistry and Physics*, 13(5), 2381–2390.
- Tegen, I., & Schulz, M. (2014). Numerical dust models Numerical dust models. In *Mineral Dust Mineral dust* (pp. 201–222). Springer.
- Todd, M., Allen, C. T., Bart, M., Bechir, M., Bentefouet, J., Cavazos-Guerra, C., et al. (2013). Meteorological and dust aerosol conditions over the western Saharan region observed at Fennec Supersite-2 during the intensive observation period in june 2011. *Journal of Geophysical Research: Atmospheres*, 118, 8426–8447. <https://doi.org/10.1002/jgrd.50470>
- Todd, M. C., & Cavazos-Guerra, C. (2016). Dust aerosol emission over the Sahara during summertime from Cloud-Aerosol Lidar with Orthogonal Polarization (CALIOP) observations. *Atmospheric Environment*, 128, 147–157.
- Todd, M. C., Washington, R., Raghavan, S., Lizcano, G., & Knippertz, P. (2008). Regional model simulations of the Bodélé low-level jet of northern Chad during the Bodélé Dust Experiment (BoDEx 2005). *Journal of Climate*, 21(5), 995–1012.
- Trzeciak, T. M., Garcia-Carreras, L., & Marsham, J. H. (2017). Cross-Saharan transport of water vapor via recycled cold pool outflows from moist convection. *Geophysical research letters*, 44, 1554–1563. <https://doi.org/10.1002/2016gl072108>
- Vanderwende, B. J., Lundquist, J. K., Rhodes, M. E., Takle, E. S., & Irvin, S. L. (2015). Observing and simulating the summertime low-level jet in central Iowa. *Monthly Weather Review*, 143(6), 2319–2336.
- Vizy, E. K., & Cook, K. H. (2009). A mechanism for African monsoon breaks: Mediterranean cold air surges. *Journal of Geophysical Research*, 114, D01104. <https://doi.org/10.1029/2008JD010654>
- Wagner, R., Schepanski, K., Heinold, B., & Tegen, I. (2016). Interannual variability in the Saharan dust source activation toward understanding the differences between 2007 and 2008. *Journal of Geophysical Research: Atmospheres*, 121, 4538–4562. <https://doi.org/10.1002/2015jd024302>
- Washington, R., Todd, M. C., Engelstaedter, S., Mbainayel, S., & Mitchell, F. (2006). Dust and the low-level circulation over the bodélé Depression, Chad: Observations from BoDEx 2005. *Journal of Geophysical Research*, 111, D03201. <https://doi.org/10.1029/2005JD006502>
- Washington, R., Todd, M., Middleton, N. J., & Goudie, A. S. (2003). Dust-storm source areas determined by the total ozone monitoring spectrometer and surface observations. *Annals of the Association of American Geographers*, 93(2), 297–313.
- Woodward, S. (2011). Mineral dust in HadGEM2 (*Hadley Centre Technical Note*). Met Office.
- Zender, C. S., Miller, R., & Tegen, I. (2004). Quantifying mineral dust mass budgets: Terminology, constraints, and current estimates. *Eos, Transactions American Geophysical Union*, 85(48), 509–512.